UNIVERSITÀ DEGLI STUDI DI PADOVA

Dipartimento di Fisica e Astronomia "Galileo Galilei"

Master Degree in Astrophysics and Cosmology

Final Dissertation

Gas and dust evolution in the circumprimary disk in binary stars

Thesis Supervisor:
Prof. Francesco Marzari

Candidate:
Utkrist Ghimire

Academic year 2021/2022

Abstract

In recent years, the discovery of numerous exoplanets in multiple stellar systems has made binaries one of the main topics in planet formation research. Despite detecting approximately a dozen planets orbiting one star in close binary systems in an S-type orbit, the standard model of planet formation is unlikely to explain their formation. Investigating the evolution of disks in close binaries can provide insight into the potential mechanisms involved in the formation of planets in such systems. In this work, we aim to investigate how the presence of a secondary star in a binary system affects the dynamics of the gas and dust that surrounds the primary star. We use the γ Cephei binary star system as a reference model to simulate and study these effects. We perform two-dimensional hydrodynamical simulations using a modified version of the FARGO3D code to model disks in close binaries. In particular, we study the evolution of gas and dust particles of different sizes (100μm, 1mm, and 1cm) over several thousand years (up to 108 kyr), specifically when the secondary star is at less perturbing configurations (the apocenter) and highly perturbing configurations (the pericenter). Our simulation confirms that when the secondary star passes through the pericenter, these perturbations result in the formation of two strong spiral arms within the disk structure. As it reaches the apocenter, the tidal forces diminish, and the disk transitions towards axisymmetric structures, damping the spiral arms. Additionally, we identified over-dense regions within the spiral arms formed during the pericenter passage, where there could be accelerated dust growth via coagulation leading to the formation of larger bodies like pebbles and planetesimals. Furthermore, we compute the mass accretion rate onto the primary star when the secondary star passes through the pericenter and when it reaches the apocenter. We found that viscous mass accretion dominates at the apocenter, leading to mass transfer onto the primary star. While at pericenter, mass is dragged away by the spiral waves. However, further detailed simulations and observations are necessary to fully comprehend the impact of these effects on circumprimary disks and planet formation in close binaries.

Contents

Chapter 1

Introduction

Sir Arthur C. Clark, best known for his Space Odyssey series, once said :

"Two possibilities exist: either we are alone in the universe or we are not. Both are equally terrifying."

This prospect has been a driving force for astronomers to study how planets are formed and search for planets that potentially harbour life beyond our Solar System. Since the discovery of extra-solar planets in the 1990s, various astronomical programs have been focusing Sun-like stars, as our Sun is the only known star in the universe that host the habitable planet. Recent studies indicates that about half of these Sun-like stars exist in multiple systems with two or more stars (Raghavan et al., 2010). This suggests that the configuration of our Solar System cannot be used as a prototype for other planetary systems present in the Universe.

In the past decade, there has been a gradual increase in the discovery of exoplanets in binaries[1] (e.g. Desidera and Barbieri, 2007; Mugrauer and Neuhäuser, 2009; Hatzes, 2016; Martin, 2018). Especially, the detection of exoplanets in binaries of separation 20 AU have left us wondering how planets could have formed in such close proximity. Even though the planet formation theory for the case of a single central star is best explained by the "standard" model via core-accretion (e.g. Safronov, 1972; Mizuno, 1980; Pollack et al., 1996), it still leaves out large fraction of multiple star systems, typically a binary system. Planet formation in binaries is rather a complex process that occurs in series of stages (Haghighipour, 2011), each of them are believed to be affected in different ways by the perturbations from the stellar companion. This underlines the importance of studying the planet formation in the binary environment.

[1] A detailed list of all planets in binary star systems can be found in: https://adg.univie.ac.at/schwarz/bincat_binary.html

The primary objective of this study is to examine the evolution of circumprimary disks within binary star systems using hydrodynamical simulations. The goal is to investigate how the presence of a stellar companion can impact the dynamics of the gas and dust surrounding the primary star during the initial phases of the planet formation process.

This thesis is divided as follows. The remainder of Chapter 1 will outline binary star systems, followed by an exploration of how a stellar companion in a close binary system can affect the planet formation process. Additionally, it will present sources that cause the dynamical evolution of planets in binaries, before discussing about protoplanetary disks. Chapter 2 is dedicated to thoroughly presenting the theoretical background of the protoplanetary disk. Chapter 3 will focus on the method used in our simulations, explaining both codes and some important governing equations. The results of our simulations will be discussed in Chapter 4, followed by conclusions of the study in Chapter 5.

1.1 Binary Stars

A binary star is a system of two stars that are gravitationally bound to one another and orbit a common center of gravity. We can generally classify binary stars in two types of system: wide binaries where stars are bound gravitationally but evolve mainly as single stars and close binaries where stars, with separation of around 20 AU, are able to affect each other's course of evolution (also known as interacting binaries Hilditch, 2001). In fact, exploring planets in binary star systems would provide us an opportunity to investigate and validate theories regarding planet formation in multiple stellar systems. Various studies relating to the planets in both single and binary star systems have confirmed that the occurrence rate of planets in single star systems is similar to that of wide binaries (see Raghavan et al., 2006; Bonavita and Desidera, 2007). This implies that the process of planet formation in wide binaries is similar to that of a single-star system, as the presence of the distant stellar companion does not seem to have a significant impact on it. On the other hand, there seems to be fewer but more massive planets orbiting binaries with separations of less than 100 AU as compared to the single-system stars (see Eggenberger et al., 2007; Bonavita and Desidera, 2007; Duchêne, 2010). However, this trend might vary with the increase in the discovery of exoplanets in close binaries.

There are various methods to identify binary stars. For instance, we can observe them using the Doppler shift in the spectral lines caused by the binary motion or

by astrometric technique to measure the wobbling of the light source around their common barycenter or even through the observed periodic variation in luminosity for an eclipsing binary.

1.1.1 Planets in binary systems

There are mainly two types of configuration for planets in binary system: S-type planets where they orbit only one star of the binary system (also known as circumprimary or circumsecondary planets) and P-type planets where they orbit both stars present in the system (also known as circumbinary planets) (see Figure 1.1).

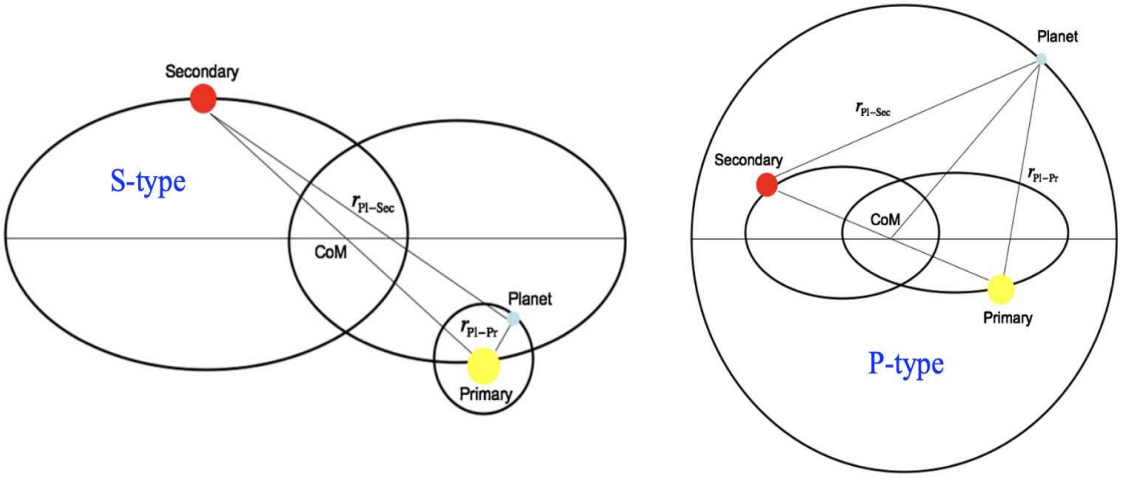

Figure 1.1: General schematic representation of the S-type system (Haghighipour and Kaltenegger, 2013) and P-type system (Kaltenegger and Haghighipour, 2013).

The increase in detection of exoplanets in multi-star systems have led to numerous studies concerning the origin of P-type planets (e.g. Kley and Haghighipour, 2014; Bromley and Kenyon, 2015) as well as S-type planets (e.g. Haghighipour, 2006; Haghighipour and Raymond, 2007; Thebault et al., 2008, 2009). In addition, Holman and Wiegert (1999) investigated the long term orbital stability of these planets in binaries by deriving empirical relation for orbital stability as a function of binary semi-major axis, mass ratio and eccentricity. In this thesis, we will solely focus on the S-type planets orbiting in close binaries.

1.1.2 S-type planets

As mentioned earlier, the planet formation in close binary system is much more challenging and vast. Until now, there has been several planets detected in a S-type

orbit in a close binary system ($a_b \lesssim 20$ AU) such as γ Cephei (Campbell et al., 1988; Hatzes et al., 2003), HD 41004 (Zucker et al., 2004), HD 196885 (Correia et al., 2008) and α Centauri (Dumusque et al., 2012). The origin of planets in these close binaries seems highly unlikely through the standard process of planet formation, as the presence of the nearby companion star would disrupt the environment significantly. Therefore, it is essential to develop comprehensive theory on planet formation that accounts for all kinds of planetary system.

There are various ways in which a stellar companion in close binary can affect the planet formation process. Firstly, the massive gaseous protoplanetary disc can be tidally truncated by the companion star (Artymowicz and Lubow, 1994; Savonije et al., 1994). The truncation radius of the disk depends on the viscosity of the disk, mass ratio of the stars and the orbital eccentricity of the binary system. This disk truncation due to tidal torques of the companion star can cause major problems for the formation of planets in close binaries. One possible problem would be the total mass present in the truncated disk might not be enough to form planets. In addition, the viscous evolution are much faster in the truncated discs as compared to the extended ones. As a consequence, these kind of disk are short-lived and hence, there might not be enough time for a planet to form. However, for the specific case of the γ Cephei system, Jang-Condell et al. (2008) found that there is sufficient material left in the truncated disk to form a observed giant planet assuming reasonable estimate for the disc's accretion rate (greater than 10^{-7} $M_\odot$ yr^{-1}) and low values of the viscosity parameters.

Secondly, the presence of the secondary star in the system may raise the disk's temperature affecting the condensation of small grains present in the disk, which eventually grows into larger pebbles and potentially kilometer-sized planetesimals. Nelson (2000) demonstrated that, for an equal-mass binary with a separation of 50 AU, the temperature in the disk may remain above the threshold necessary to facilitate grain condensation. This findings were later confirmed by Picogna and Marzari (2013) through three-dimensional modeling of radiative disks. They identified significant heating of the disk due to the development of spiral shock wave when the stars approach their pericenter, as well as mass transfer between the two disk of the system (see Figure 1.2).

Additionally, the presence of a secondary star in an eccentric orbit can periodically cause gravitational perturbation to the disk, leading the disk around the primary star to also become eccentric (Kley and Nelson, 2008; Paardekooper et al., 2008). As the disk eccentricity increases, the collision velocities between planetesi-

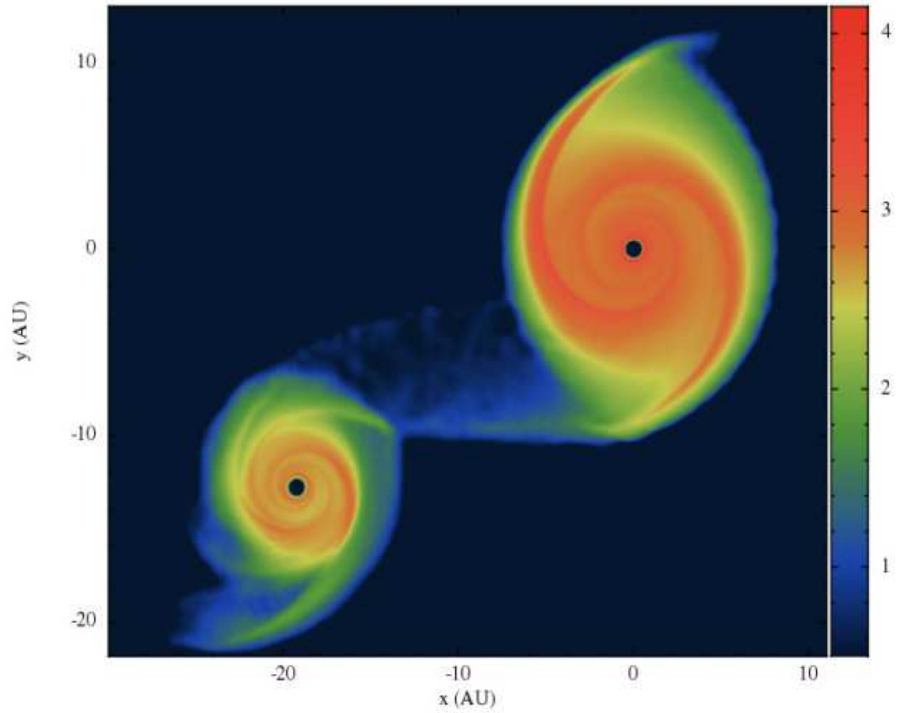

Figure 1.2: Illustrating superficial density on a logarithmic scale of a circumstellar disk during the secondary star's pericenter passage (Picogna and Marzari, 2013).

mals also increases (Müller and Kley, 2012) making the collisions more disruptive. As a result, the planet formation through the planetesimal collisions would be particularly challenging. However, the presence of a gas disk can drastically change the whole scenario. Marzari and Scholl (2000) showed that the gas drag force along with the periodic perturbation by the companion star can greatly decrease the impact velocities of planetesimals even when there is high orbital eccentricity.

1.1.3 Dynamics of planets in binaries

In a binary star system, the gravitational influence of the secondary star plays a pivotal role in shaping not only the initial planet formation but also the subsequent dynamic changes. The eventual final structure of the system heavily depends on how the evolutionary paths of planets are altered by factors such as disk interactions (Kley and Nelson, 2010), Mean Motion Resonances (MMR) between planets and between planets and the secondary star (Deck et al., 2013; Mudryk and Wu, 2006), planet interactions causing scattering (Marzari et al., 2005), and the Kozai mechanism (Naoz, 2016).

For planets in S-type orbits, revolving around one of the stars, the most critical areas for planet formation are the outer regions. In these regions, the gravitational pull of the second star might trigger significant eccentricities, possibly leading to instability due to resonance interactions. Additionally, if the planetary orbits are misaligned, the secondary star could induce rapid Kozai oscillations, causing substantial variations in eccentricity and inclination (Marzari and Thebault, 2019). While these mechanisms can collectively or independently influence the evolution of planetary systems within binaries, secular perturbations (Michtchenko and Malhotra, 2004; Libert and Henrard, 2005) and Mean Motion Resonances (MMR) play a significant role in establishing the outer boundary where a planet's orbit remains stable within an S-type configuration. Conversely, the inner regions of the circumstellar disk offer a more favorable environment for planet growth through the standard core-accretion process, fostering subsequent stability in their orbital trajectories.

In P-type orbits, where planets orbit both stars, disruptions are more likely in the inner regions near the central binary. In this configuration, instability is expected closer to the system's center, with the safer zones for planet formation lying in the outer regions of the encircling binary disk (Marzari and Thebault, 2019).

1.2 Protoplanetary disk

Stars are formed when a large rotating cloud consisting of cold and dense molecular gas begins to collapse due to self-gravity. As a consequence of angular momentum conservation in this rotational-collapse process, the molecular cloud cannot fall spherically onto the star. Rather, the material surrounding the young star forms a disk where planet forms known as protoplanetary disk. While some part of gas and dust particles present in the disk spiral inward and accrete onto the protostar, remaining material in the disk ends up growing into pebbles and planetesimals to

form planets (Pollack et al., 1996). Since protoplanetary disk consist of materials that is initially present in the interstellar medium, it is mainly composed of hydrogen and helium (99% by mass) and 1% of dust (Bohlin et al., 1978).

The existence of the protoplanetary disk were discovered long ago by studying the spectral energy distribution (SED) of young stellar objects (YSO). In addition to the blackbody radiation emitted by the star, the heated dust present in the disk contributes to an excess signal at long wavelengths (infrared excess). In particular, the slope of the SEDs help us quantify the infrared excess by classifying YSOs (Andre, 2000):

$$\alpha_{IR} = \frac{dlog(\lambda F_\lambda)}{dlog(\lambda)} \tag{1.1}$$

YSOs are divided into four different classes based on the shape of their SEDs, which depicts a distinct evolutionary stage of the protoplanetary disk (see Figure 1.3). These classes are often referred to as Class 0, Class I, Class II and Class III.

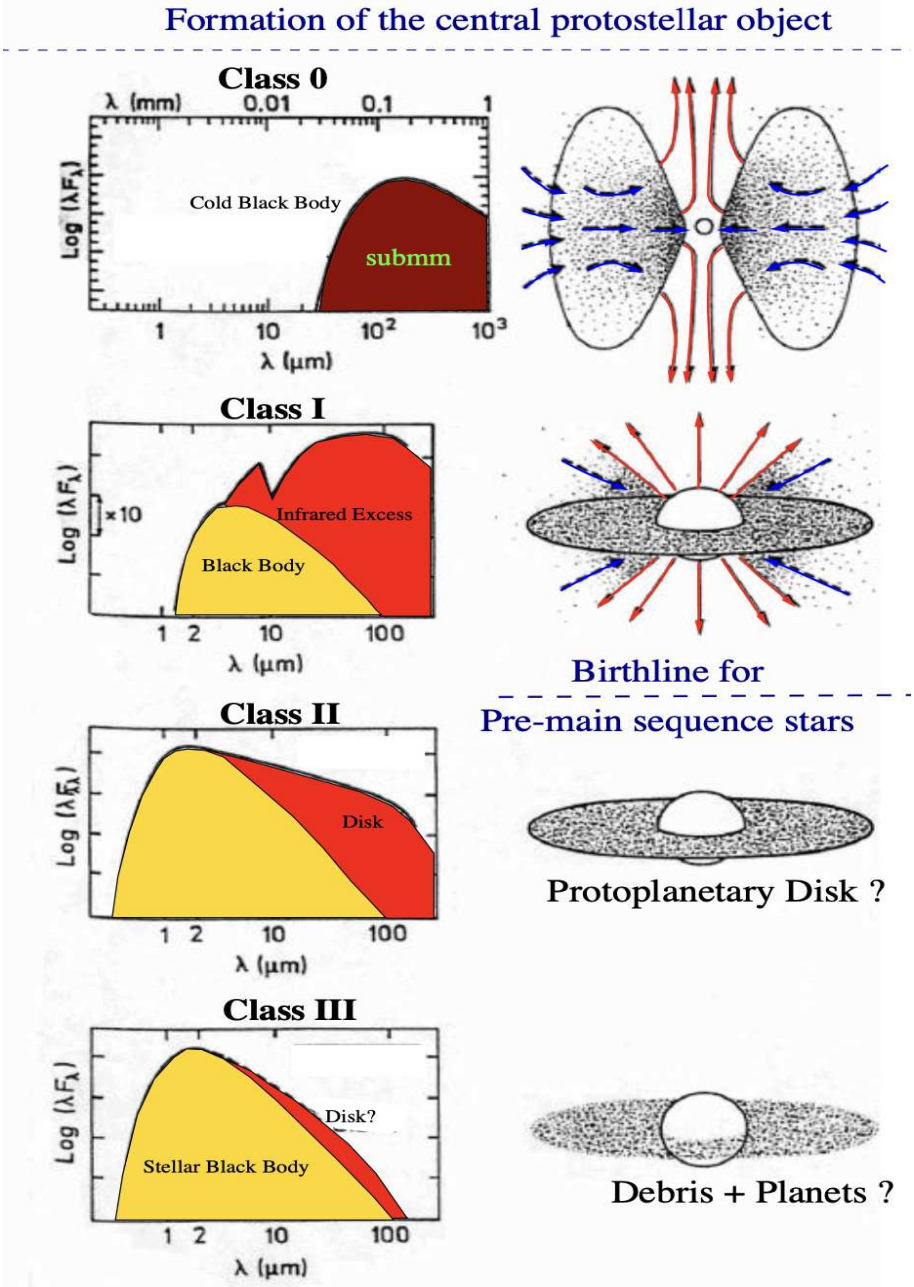

Figure 1.3: A step-by-step observational evolutionary sequence outlining the formation of a single star, starting from a prestellar cloud core and progressing to a Class III Young Stellar Object (YSO), based on the shape of the SED (Andre, 2000).

In addition, the infrared excess also helps in deducing the so called "transition disks". These type of disks are primarily in an advanced evolutionary stage where dust-depleted cavity develops in the central region of the disk. These disks have mainly progressed to an advanced evolutionary stage, marked by the formation of a cavity in the central area that lacks dust particles.

In the past decade, there has been a huge progress in observing protoplanetary disks. The structures in protoplanetary disks around young stars have been spacially resolved in optical and near-infrared wavelengths by the Spectro-Polarimetric High-contrast Exoplanet REsearch (SPHERE) instrument (Beuzit et al., 2008) mounted on ESO's Very Large Telescope (VLT) located in Chile. In particular, gas and small dust particles present in the disks are able to modify the light rays via scattering, absorption and remission. With the help of this instrument, we are able to obtain scattered light images from the surface of protoplanetary disks in infrared wavelengths. However, it can be very challenging to observe the structure of the disks at optical and infrared wavelengths, as the central star also emits at the same wavelength range. By applying two special techniques: the polarized differential imaging technique (PDI, Kuhn et al., 2001; Apai et al., 2004) and the angular differential imaging technique (ADI, Marois et al., 2006), the SPHERE instrument is able to get rid of the incoming flux from the central star and finally able to conduct a detailed study of protoplanetary disk (see Figure 1.4).

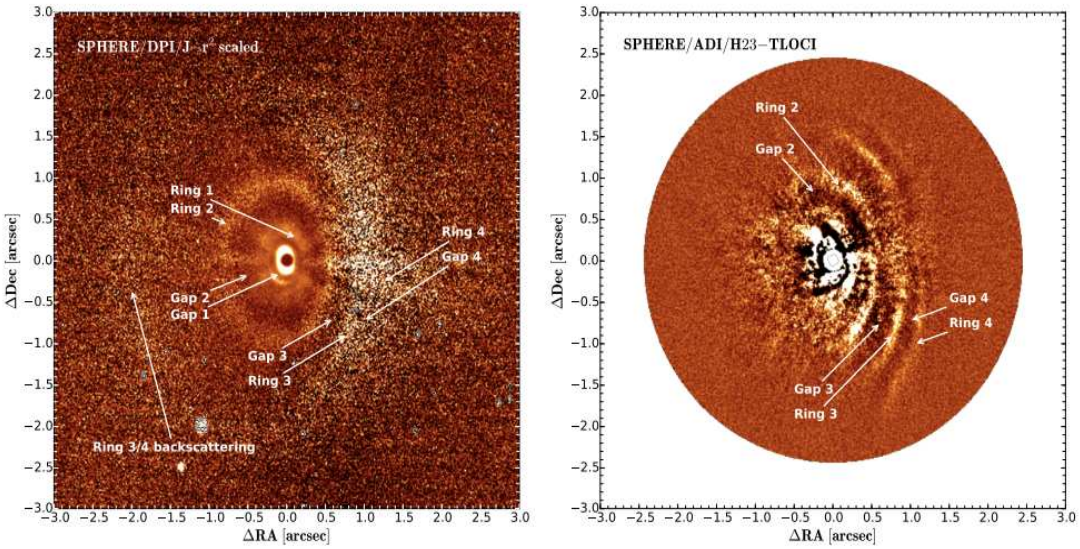

Figure 1.4: SPHERE/IRDIS PDI (left) and ADI (right) images of HD 97048. The disk structure is identified, with signal detected at the positions of the two outermost rings found in the ADI image, as seen in the r^2-scaled DPI image (Ginski et al., 2016).

Tiny particles of dust scatter light and also have the ability to absorb photons, which results in heating of the particles in the disk. This heat is then emitted in the form of millimeter and sub-millimeter wavelengths. The Atacama Large Millimeter/submillimeter Array (ALMA) interferometer, situated in Chile, consisting of 66 highly sensitive telescope dishes operating at wavelengths of 3.6 to 0.3 millimeters, now allows us to measure the emission of dust continuum, which can trace the presence of dust particles in the disk's mid-plane. With ALMA interferometer, it is now possible to obtain large sample of high-resolution images of disks in different stellar clusters and regions where stars are formed (see Figure 1.5). These images are able to highlight key attributes such as gaps, spiral waves, and inner holes in the disks. Additionally, ALMA has allowed us to make statistical estimates regarding the proportion of stars possessing disks and their lifetimes.

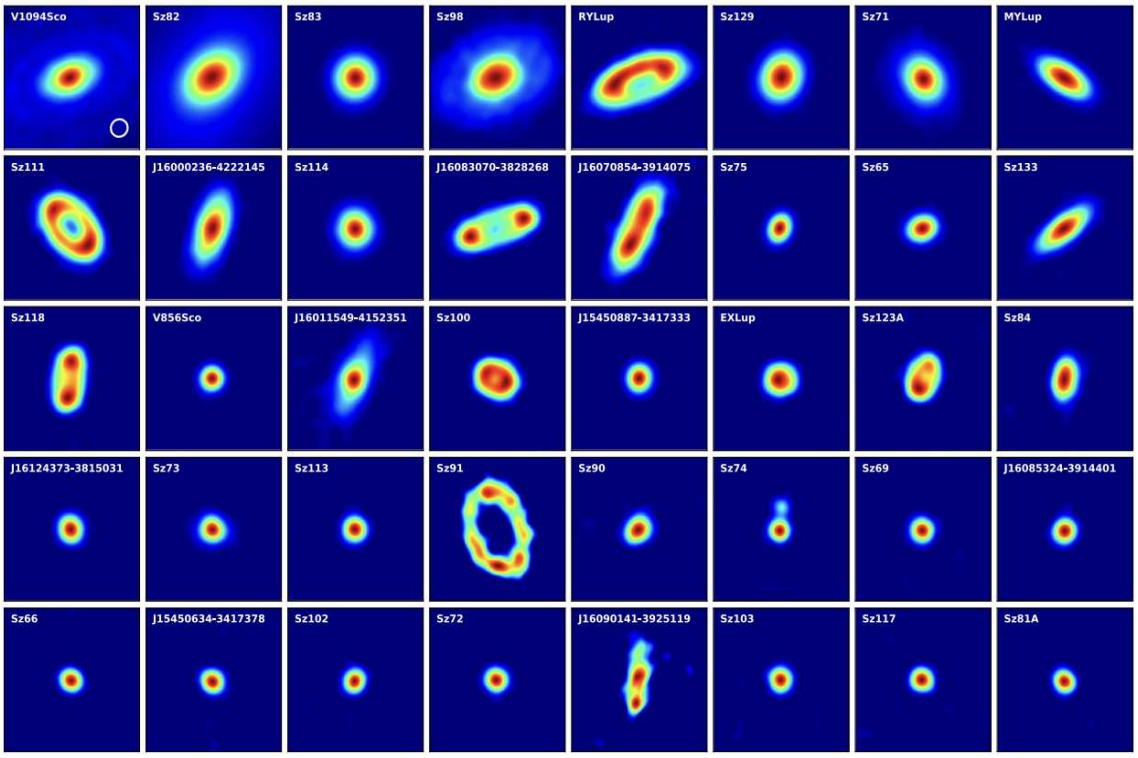

Figure 1.5: 1.33 mm continuum images of the 40 Lupus disks detected in ALMA Band 6 sample (Ansdell et al., 2018).

Chapter 2

Physics behind protoplanetary disks

Eventhough the observations presented in the previous section provides valuable insight into potential planetary and protoplanetary environments, it is important to note that it only offers a glimpse into the current state of these systems, and to truly comprehend their development over time, it is necessary to rely on theoretical frameworks that can help us understand the underlying processes and mechanisms that drive their evolution.

In the following section, we will discuss about the theoretical concepts of protoplanetary disks and the dynamics governing the evolution of gas and dust particles which together lay the foundation for this thesis.

2.1 Gaseous structure of the disk

Protoplanetary disks, the cradle of a future planetary system, are the by-product of the star formation process. The structure of these gas-rich disks is quite complex, and various physical processes are involved in different parts of the disk (see Figure 2.1). These disks can expand over a wide range of distances, with the outer edge ranging from a few tens of AU to 100 AU or more, and the inner edge located as close as few stellar radii. The lifetime of protoplanetary disks typically spans a few million years, which corresponds to millions of dynamical timescales in the inner region and thousands of dynamical timescales in the outer region of the disk, specifically at a distance of 100 AU.

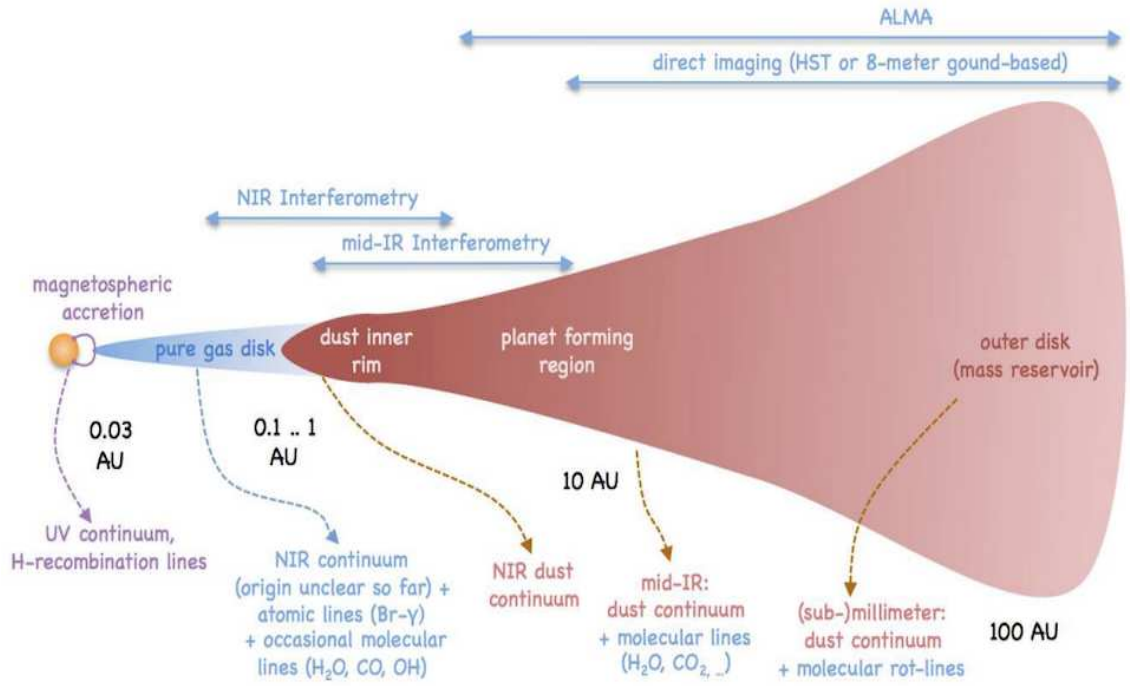

Figure 2.1: This general diagram depicts the structure of a protoplanetary disk and its associated spatial scales. It shows the techniques that can resolve specific scales, and also indicates the emission types corresponding to different parts of the disk (Dullemond and Monnier, 2010).

2.1.1 Vertical structure

A vertical structure of the gas disk can be derived by first assuming that the total disk mass, M_{disk} is very small compared to the mass of the star, $M_\star$. This would allow us to neglect the gravitational potential of the disk and solely focus on stellar gravity. Secondly, we consider the disk to be vertically isothermal (i.e. the vertical temperature profile, $T(z)$ is constant) and thin (i.e. the vertical thickness above the mid-plane of the disk, z is a very small compared to the orbital radius, r). The equilibrium structure is determined by the balance between vertical component of the stellar gravity, g_z and vertical pressure gradient in the gas, $\frac{1}{\rho}\frac{dP}{dz}$ (see Figure 2.2).

Therefore, we can write:

$$\frac{dP}{dz} = -\rho g_z = -\rho g \sin\theta \tag{2.1}$$

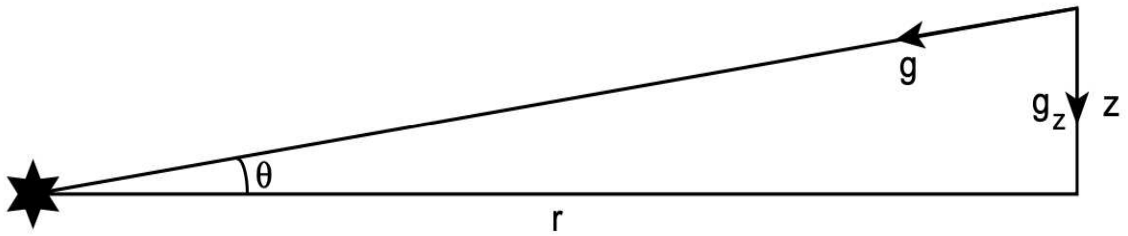

Figure 2.2: This diagram illustrates the geometry used to determine the vertical hydrostatic equilibrium of a protoplanetary disk that is not influenced significantly by its own gravitational forces. The equilibrium is maintained by the vertical component of stellar gravity and the vertical pressure gradient (Armitage, 2020).

This implies,

$$ {c_s}^2 \frac{d\rho}{dz} = -\rho \frac{GM_\star z}{(r^2 + z^2)^{3/2}} \tag{2.2} $$

where, $P = \rho {c_s}^2$ with c_s being the speed of sound.
For a thin disk $z << r$, $g_z \simeq \Omega_K^2$ where Ω_K^2 is the Keplerian orbital velocity at the mid-plane of the disk. Then, the equation becomes

$$ {c_s}^2 \frac{d\rho}{dz} = -\Omega_K^2 \rho z \tag{2.3} $$

Integrating above equation would give a Gaussian density profile of the gas,

$$ \rho(z) = \rho_0 \exp[-z^2/2h^2] \tag{2.4} $$

where, $h \equiv c_s/\Omega_K$ is the vertical scale height and $\rho_0 = \frac{1}{\sqrt{2\pi}} \frac{\Sigma}{h}$ is the gas density at the mid-plane, with Σ being the gas surface density.

2.1.2 Radial structure

Protoplanetary disks are dynamic systems, and determining the surface gas-density profile of the disk in the radial direction requires an understanding of the transfer of angular momentum, often referred to as viscosity (see Section 2.1.4), or through direct observations of the disk.

Angular momentum transport occurs when two adjacent layers of gas in the disk experience friction due to their relative motion. In the disk, the gas moves in

a Keplerian motion around the central star, with the gas in the inner layer rotating faster than the gas in the outer layer. This generates a viscous friction, which causes the inner layer to slow down and the outer layer to speed up. This allows the local parcels of gas in the inner layer to spiral toward the central star by reducing its angular momentum, while the gas in the outer layer moves further away from the central star by gaining its angular momentum. This internal redistribution of angular momentum is not the only way how disk evolves; magnetic stresses can also remove angular momentum, enabling matter to accrete, even without viscosity (Blandford and Payne, 1982) or disk winds may also play a role in its evolution.

In this thesis, we focus on the evolution of the disk over long periods; hence, we are only interested in the time evolution of the surface density.

2.1.3 Surface density evolution of the disk

We start by assuming the disk to be evolving slowly through the sequence of axisymmetric-static[2] structures. The evolution of gas surface density, $\Sigma(r,t)$ can be derived by considering the mass and angular momentum conservation equations in cylindrical coordinates. The continuity equation that expresses mass conservation is given by,

$$r\frac{\partial \Sigma}{\partial t} + \frac{\partial}{\partial r}(r\Sigma v_r) = 0 \tag{2.5}$$

and, the azimuthal component for angular momentum conservation is expressed as,

$$r\frac{\partial}{\partial t}(r^2\Omega\Sigma) + \frac{\partial}{\partial r}(r^2\Omega \cdot r\Sigma v_r) = \frac{1}{2\pi}\frac{\partial G}{\partial r} \tag{2.6}$$

Here, v_r is the radial velocity of the gas ($v_r < 0$ corresponds to inflow towards the star), Ω is the angular velocity of the gas and G is the torque exerted on the disk, which can be expressed as,

$$G = 2\pi r \cdot \nu\Sigma r\frac{d\Omega}{dr} \cdot r \tag{2.7}$$

with ν being kinematic viscosity.

[2] A three-dimensional structure is defined as "axisymmetric" if its geometry, physical characteristics and boundary conditions are independent of an azimuth coordinate, θ of a cylindrical reference frame (r, θ, z), where z is the component axis of symmetry and r is the radial distance from z-axis. This simplifies the problem to a two-dimensional plane in the radial and vertical dimensions.

The change in the angular momentum of a disk can be attributed to two factors: firstly, the change in the surface density due to radial flows, and secondly, the difference in the amount of torque exerted on the disk by stresses at its inner and outer edges. Solving the above two equations 2.5 and 2.6, we then obtain the evolution of the gas surface density of the thin disk, and can be written as,

$$\frac{\partial \Sigma}{\partial t} = \frac{3}{r}\frac{\partial}{\partial r}\left[r^{1/2}\frac{\partial}{\partial r}(\nu \Sigma r^{1/2})\right] \tag{2.8}$$

And, the radial velocity of the gas in the presence of a viscosity can also be derived as,

$$v_r = -\frac{3}{\Sigma\sqrt{r}}\frac{\partial}{\partial r}(\Sigma \nu \sqrt{r}) \tag{2.9}$$

Substituting $x = 2\sqrt{r}$ and $y = \Sigma\sqrt{r}$ in equation 2.8, we can obtain a diffusion equation:

$$\frac{\partial y}{\partial t} = D\frac{\partial^2 y}{\partial x^2} \tag{2.10}$$

with D being a diffusion constant such that,

$$D = \frac{12\nu}{x^2} \quad \text{(assuming a constant viscosity)} \tag{2.11}$$

We can then determine a timescale on which viscosity would smooth out surface density gradients in a disk of size r:

$$t_{visc} = \frac{x^2}{D} \sim \frac{r^2}{\nu} \tag{2.12}$$

known as viscous timescale, t_{visc} of the disk. An analytic solutions to the time-dependent diffusive equation 2.5 can help us gain insight on how the gas surface density varies with radius at different times for different forms of the viscosity (see Figure 2.3).

2.1.4 Impact of the viscosity on disk evolution

The rate at which the disk evolves and its density distribution are both influenced by how angular momentum is transported within the disk. This transport is primarily controlled by the viscosity of the disk, making it a crucial parameter in this

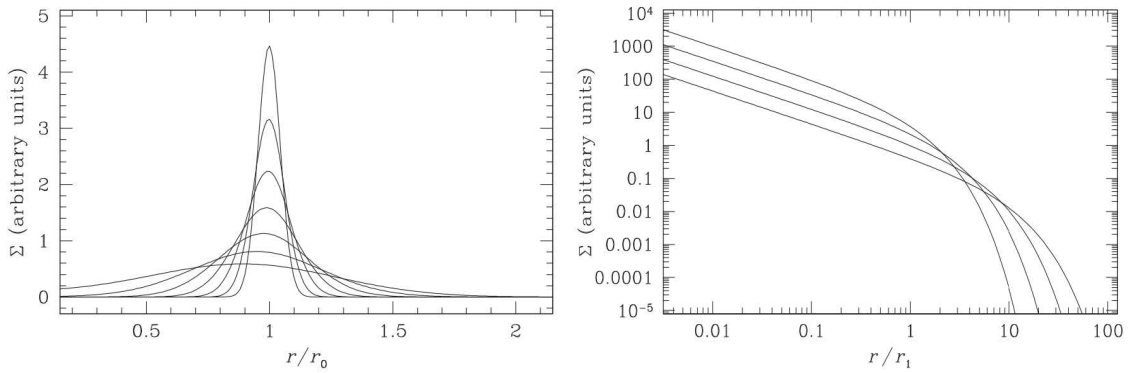

(a) ν is constant. **(b)** $\nu \propto r$.

Figure 2.3: Variation of gas surface density with radius at different times for different forms of viscosity (Armitage, 2020).

process. One possible mechanism for generating viscosity in a gas disk is through the interaction between different molecules in the gas, which is known as molecular viscosity, ν_m. Therefore, this type of viscosity generated via colliding molecules in the gas disk is given by,

$$\nu_m \sim \lambda v_{th} \tag{2.13}$$

where, v_{th} is the thermal speed of the molecules and $\lambda \sim \dfrac{1}{n\sigma}$ is the mean-free path in the gas, with n being the number density of molecules having collision cross-section σ.

Considering the collision cross-section to be the size of a hydrogen molecule (i.e. $\sigma \sim 2 \times 10^{-15} cm^2$) and under appropriate physical conditions at 10 AU (i.e. $v_{th} = 0.5\ kms^{-1}$, $n = 10^{12}\ cm^{-3}$), we can estimate the molecular viscosity, ν_m to be around $2.5 \times 10^7\ cm^2 s^{-1}$ (adopted from Armitage, 2020). We can then infer the viscous time scale to be:

$$t_{visc} \simeq \frac{r^2}{\nu_m} = 3 \times 10^{13} yr \tag{2.14}$$

This time scale is much longer than the observed time scale for the disk evolution. Therefore, molecular viscosity is not the mechanism responsible for the angular momentum transport within disks.

Undoubtedly, we need another mechanism for the angular momentum transport that can explain the observed disk lifetimes. Shakura and Sunyaev (1973) have put forward the idea of turbulence playing the key role in providing viscosity for the angular momentum transport. We can therefore express the turbulent viscosity, ν

in terms of the sound speed, c_s and disk scale-height, h as,

$$\nu = \alpha c_s h \tag{2.15}$$

where, the dimensionless parameter, α describes the amount of turbulence in the disk, which may vary with different density and temperature profile, as well as the distribution of the gas within the disk.

2.1.5 Mass accretion rate on the star

In a simple viscous disk, the rate at which the material in the inner regions of the disk falls onto the central star due to the loss of angular momentum is known as mass accretion rate on the star. To account for the angular momentum lost by the accreting material, the disk must expand. Therefore, the evolution of the disk can be predicted based on the rate of mass accretion and angular momentum transfer, which is proportional to the viscosity of the disk.

We can derive a relation between the mass accretion rate to the viscosity value in the disk by starting from the angular momentum conservation equation,

$$r\frac{\partial}{\partial t}(r^2\Omega\Sigma) + \frac{\partial}{\partial r}(r^2\Omega \cdot r\Sigma v_r) = \frac{1}{2\pi}\frac{\partial}{\partial r}\left(2\pi r \cdot \nu\Sigma r\frac{d\Omega}{dr} \cdot r\right) \tag{2.16}$$

We can look for a steady-state solution to the above equation 2.16, where the local superficial density, Σ is assumed to be constant. For this, we set the time derivative to zero, we get,

$$\frac{\partial}{\partial r}(r^2\Omega \cdot r\Sigma v_r) = \frac{1}{2\pi}\frac{\partial}{\partial r}\left(2\pi r \cdot \nu\Sigma r\frac{d\Omega}{dr} \cdot r\right) \tag{2.17}$$

From the definition of the mass accretion rate, $\dot{M}$, we can write,

$$\dot{M} = -2\pi r\Sigma v_r \tag{2.18}$$

Inserting this expression in the equation 2.17 and integrating from the radius of the star, $r_\star$ (assuming it to be the inner limit of the disk) to the radial distance, r, we obtain,

$$-\dot{M}r^2\Omega = 2\pi\nu\Sigma r^3\frac{d\Omega}{dr} + constant \tag{2.19}$$

To specify *constant*, we set $\frac{d\Omega}{dr} = 0$, as the viscous stress vanishes on the surface of the star. we have,

$$constant = -\dot{M} r_\star^2 \Omega(r_\star) \tag{2.20}$$

Finally, the steady-state solution for the disk can be expressed as,

$$\dot{M}\left(1 - \sqrt{\frac{r_\star}{r}}\right) = 3\pi\nu\Sigma \tag{2.21}$$

For the majority of the disk where $r >> r_\star$, the mass accretion rate on the star is given by,

$$\dot{M} = 3\pi\nu\Sigma \tag{2.22}$$

Furthermore, there is a strong correlation between the mass of the central star and the rate at which it accretes mass, with larger stars typically possessing more massive disks experience a higher rate of mass accretion (see Figure 2.4).

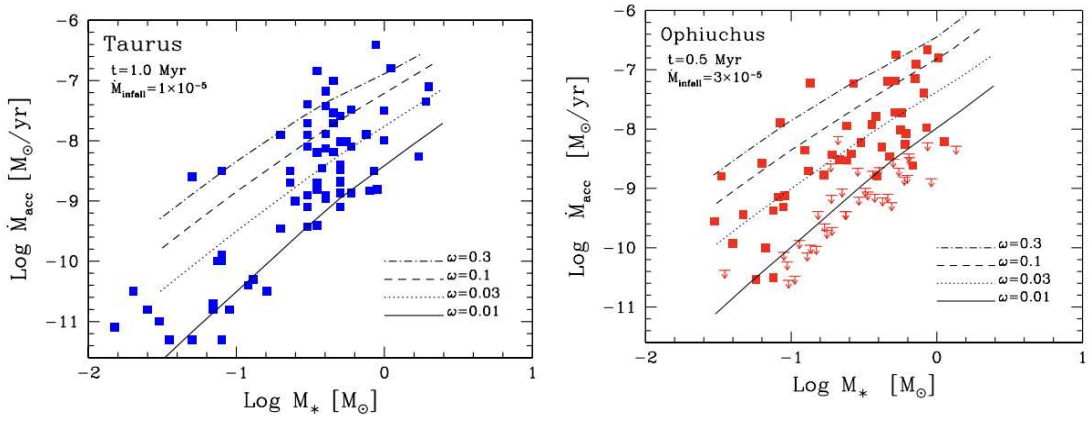

Figure 2.4: The diagram illustrates how the mass accretion rate, $\dot{M}_{acc}$ varies with the mass of the central object, M_* in Taurus (left panel) and ρ Oph (right panel) (Dullemond et al., 2006).

2.2 Dust dynamics of the disk

Let us now focus on the evolution of dust particles within the disks, which is quite different from the evolution of the dominant gaseous component in the disk. Although the disk consists of a small fraction of solid particles (about 1% of the total

disk's mass), it still has a significant impact on the structure and evolution of protoplanetary disks. We will therefore begin by describing the aerodynamical interaction between the small dust particles and gas to understand how such particles evolve vertically and radially within the protoplanetary disk.

2.2.1 Aerodynamical gas-dust interaction

While gas molecules can be affected by pressure gradients, dust particles are primarily driven by the gravitational forces and the drag forces that result from their aerodynamical interaction with the surrounding gas. We will start by defining a critical parameter that quantifies the coupling between solid particles and gas, commonly referred to as the stopping time.

For a spherical solid particle with radius s having density ρ_m, the stopping time, t_s is given by,

$$t_s \equiv \frac{m\Delta v}{|F_{drag}|} \tag{2.23}$$

where, m is the mass of the particle moving with velocity v relative to the local velocity of the gas and F_{drag} is the magnitude of the aerodynamic drag force experienced by the solid particle. We now define a more meaningful parameter known as dimensionless stopping time[3], τ_s by multiplying t_s by the local Keplerian angular velocity, Ω_K and is given by,

$$\tau_s \equiv t_s \Omega_K \tag{2.24}$$

The coupling between gas and dust particles can also be described in terms of dimensionless stopping time by the Stokes number, St, which can be expressed as,

$$St = \frac{\tau_s}{\tau_{ed}} \tag{2.25}$$

where, τ_{ed} is the characteristic turn-over timescale of eddies, which can be associated with turbulence in the disk. In simpler terms, large eddies with longer turn-over times are linked with larger-scale turbulent motions, while smaller eddies with shorter turn-over times represent smaller-scale turbulent fluctuations in the disk. Thus, the turn-over time scales of eddies is valuable measure that contributes to understanding the dynamics of turbulence within the disk.

[3]It explains how the stopping time and the orbital time at the particle's position are related to each other.

In particular, we will consider two different regime when calculating the drag force experienced by the solid particle:

Epstein regime: Solid particles are considered to be in this regime if they are smaller than the mean-free path of gas molecules (λ) i.e. s $< 9\lambda/4$. In this regime, gas acts as a group of collisionless molecules with Maxwellian velocity distribution towards the dust. The drag force experienced by the solid particles in this regime is known as Epstein drag and is given by,

$$F_{drag} = -\frac{4\pi}{3}\rho_{gas} s^2 v_{th} \Delta v \tag{2.26}$$

where, ρ_{gas} is the density and $v_{th} = \sqrt{\frac{8k_B T}{\pi \mu m_H}}$ is the thermal speed of the surrounding gas molecules.

Stokes regime: When particles reach a size significantly larger than the mean free path of gas molecules, their interaction with the gas can be described using classical fluid concepts, and they are considered to be in the Stokes regime. The drag experienced by the particles in this regime, also known as Stokes drag, can be expressed as follows:

$$F_{drag} = -\frac{C_D}{2}\pi s^2 \rho_{gas} v_{th} \Delta v \tag{2.27}$$

where, C_D is the drag coefficient. It represents the level of resistance or drag experienced by a particle moving through a gas or fluid. Specifically, a higher drag coefficient indicates greater resistance to the motion of the solid particle, resulting in a larger drag force acting on the object. The drag coefficient is determined by various factors, including the shape and size of the particles. Moreover, it can vary depending on the Reynolds number (Re), which is defined as the ratio of inertial forces to viscous forces within a fluid flow. The Reynolds number is expressed as follows:

$$Re = \frac{2sv}{\nu_m} \tag{2.28}$$

Based on the Reynolds number, Weidenschilling (1977) presents a relation to classify fluid flow into further three different regimes:

1. Stokes I: $C_D \simeq 24 Re^{-1}$, for Re < 1.

2. Stokes II: $C_D \simeq 24Re^{-0.6}$, for $1 < \mathrm{Re} < 800$.

3. Stokes III: $C_D \simeq 0.44$, for $\mathrm{Re} > 800$.

2.2.2 Radial drift

As discussed earlier, the gas within the disk is partially supported against gravity by an outward pressure gradient, causing it to orbit the central star at a sub-Keplerian velocity. This differential velocity of the gas has significant implications for the radial distribution of the dust particles of different sizes present within the disk. We will begin by assuming that there is no turbulence in the disk and that the feedback of aerodynamic forces on the gas is negligible. To derive a general relation for the rate of radial drift as a function of the stopping time, we consider the gas orbital velocity to be:

$$v_{\phi,gas} = v_K(1-\eta)^{1/2} \quad . \tag{2.29}$$

where, the parameter $\eta \propto (h/r)^2$.

If v_r and v_ϕ is the radial velocity and the azimuthal velocity of the particle respectively, the equations of motion can be written as:

$$\frac{dv_r}{dt} = \frac{v_\phi^2}{r} - \Omega_K^2 r - \frac{1}{t_s}(v_r - v_{r,gas}) \quad , \tag{2.30}$$

$$\frac{d}{dt}(rv_\phi) = -\frac{r}{t_s}(v_\phi - v_{\phi,gas}) \quad . \tag{2.31}$$

The azimuthal equation 2.31 can be simplified by noting that the specific angular momentum remains close to Keplerian. This implies that as the particle spiral inward, it follows a series of orbits that are almost circular and nearly Keplerian in nature. Therefore,

$$\frac{d}{dt}(rv_\phi) \simeq v_r \frac{d}{dr}(rv_K) = \frac{1}{2}v_r v_K \quad . \tag{2.32}$$

yielding,

$$v_\phi - v_{\phi,gas} \simeq -\frac{1}{2}\frac{t_s v_r v_K}{r} \quad . \tag{2.33}$$

We now substitute for Ω_K in the radial equation 2.30 using equation 2.29 and also

neglect higher order terms, we get,

$$\frac{dv_r}{dt} = -\eta\frac{v_K^2}{r} + \frac{2v_K}{r}(v_\phi - v_{\phi,gas}) - \frac{1}{t_s}(v_r - v_{r,gas}) \quad . \tag{2.34}$$

Here, the term $\frac{dv_r}{dt}$ is negligible, so we omit it. Also, we replace $(v_\phi - v_{\phi,gas})$ using equation 2.33, we obtain,

$$v_r = \frac{(r/v_K)t_s^{-1}v_{r,gas} - \eta v_K}{(v_K/r)t_s + (r/v_K)t_s^{-1}} \quad . \tag{2.35}$$

Finally, the radial velocity of the particle in terms of the Stokes number is given by,

$$v_r = \frac{\tau_s^{-1}v_{r,gas} - \eta v_K}{\tau_s + \tau_s^{-1}} \quad . \tag{2.36}$$

For a small dust particle that are tightly coupled to the gas ($\tau_s << 1$), the radial drift occurs at a speed,

$$v_r \simeq v_{r,gas} - \eta\tau_s v_K \quad . \tag{2.37}$$

The small dust particles, influenced by strong aerodynamic coupling, are compelled to orbit alongside the surrounding gas molecules at the same rotational speed. However, their velocity is slower than what is required to achieve a balance between centrifugal force and gravity. As a result, the dust particles will gradually spiral inward at their radial terminal velocity. Hence, these small dust particles experience radial drift at a rate that is linear in the dimensionless stopping time.

Even when dealing with very large particles ($\tau_s >> 1$) that have weak coupling to the gas, they still experience inward radial drift at a rate that decreases linearly with the stopping time. In this situation, the aerodynamic forces acts as a disturbances to the orbital motion of the solid particle, which revolves around the central star at a velocity close to the Keplerian speed. This velocity is faster than the motion of the gas within the disk, causing the solid body to encounter a headwind that diminishes its angular momentum. Consequently, the particle gradually drifts inward. Figure 2.5 shows the radial drift time scale, t_{drift} as a function of the dimensionless stopping time.

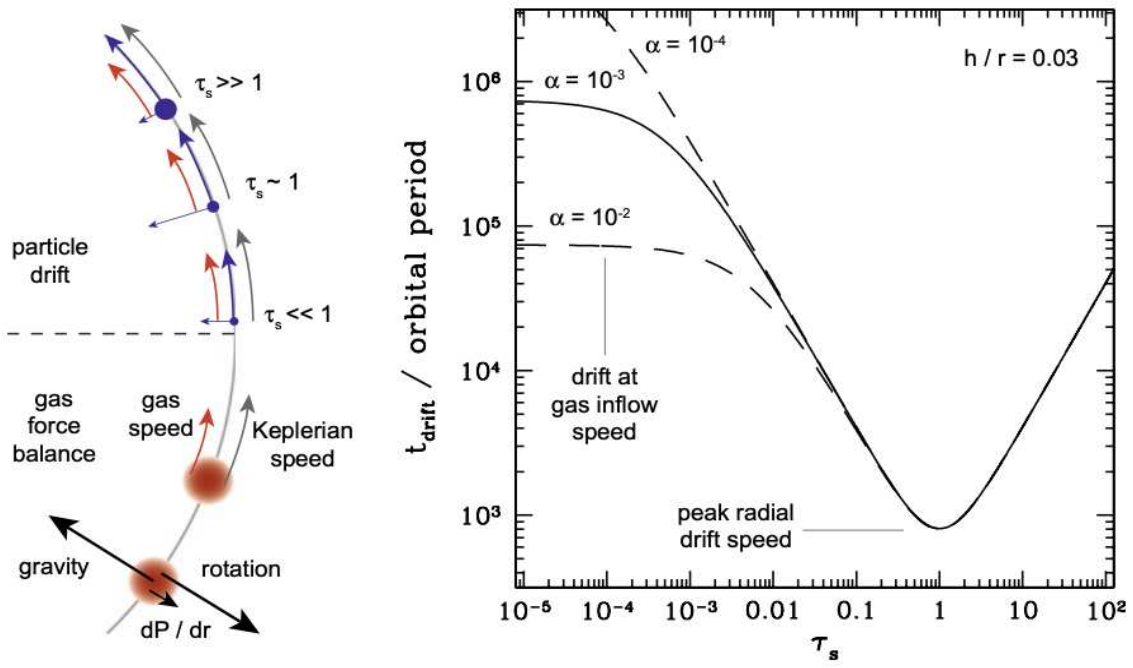

Figure 2.5: Particles in a disk migrate towards the center due to the interplay of aerodynamic forces and the sub-Keplerian rotation of the gas. The diagram demonstrates how the radial drift time scale, t_{drift} changes with respect to the dimensionless stopping time, τ_s. The highest radial drift rate happens when τ_s is equal to 1 (Armitage and Kley, 2019).

Drift in the turbulent disk

If there is turbulence within the disk, the radial drift of small particles can be significantly affected. However, large particles can still experience rapid inward drift, as turbulence does not alter the mean sub-Keplerian flow responsible for their radial motion. When modeling the radial transport of solids in a turbulent disk, three main processes need to be considered: advection with the mean flow, radial drift due to aerodynamic drag relative to the gas, and turbulent diffusion. Therefore, we begin by writing the concentration of dust or trace gas (also known as a "contaminant") as follows:

$$f = \frac{\Sigma_d}{\Sigma} \quad , \tag{2.38}$$

where, Σ_d is the surface density of the contaminant. The radial movement of the contaminants can now be described by an advection-diffusion equation as,

$$\frac{\partial \Sigma_d}{\partial t} + \nabla \cdot F_T = 0 \quad , \tag{2.39}$$

where, the total flux, F_T can be divided into two parts: an advective flux that describes the transport of particles with the mean flow of the disk and a diffusive flux that ensures the even distribution of contaminants throughout the disk. For $f \ll 1$, we can assume that the diffusive properties of the disk depend only on the gas surface density and flux can be expressed as,

$$F_T = \Sigma_d \mathbf{v} - D\Sigma\nabla\left(\frac{\Sigma_d}{\Sigma}\right) \quad . \tag{2.40}$$

where, $\mathbf{v}$ is the mean velocity of gas in the disk and D is the turbulent diffusion coefficient. The diffusive term vanishes if the contaminant is constant. Combining this flux expression with the continuity equation for the gaseous component, we obtain an evolution equation for the contaminants as,

$$\frac{\partial f}{\partial t} = \frac{1}{r\Sigma}\frac{\partial}{\partial r}\left(Dr\Sigma\frac{\partial f}{\partial r}\right) - v_r\frac{\partial f}{\partial r} \quad . \tag{2.41}$$

2.2.3 Vertical settling

Aerodynamic drag on solid particles can also alter the vertical distribution of solid particles within the protoplanetary disk. We begin by assuming there is no turbulence in the disk. Let us now focus on the forces acting on a small particle of mass, m at height, z above the mid-plane of a laminar disk. While the vertical component of stellar gravity would cause solid particles not coupled to the gas to oscillate around the mid-plane of the disk, the counteracting drag force dampens this motion, leading the particles to settle towards the disk's mid-plane. We can express the vertical component of stellar gravity, F_G (downward force) and drag force, F_{drag} in Epstein regime (upward force) as follows:

$$|F_G| = m\Omega_K^2 z \quad . \tag{2.42}$$

$$|F_{drag}| = \frac{4\pi}{3}\rho_{gas}s^2 v_{th} v \quad . \tag{2.43}$$

and, the resulting terminal settling velocity of the particle once the gravitational force is balanced by drag force is given by,

$$v_{settle} = \frac{\rho_m}{\rho_{gas}}\frac{s}{v_{th}}\Omega_K^2 z \quad . \tag{2.44}$$

Roughly estimating, for a 1 μm particle at $z \sim h$ at $1AU$ from a solar mass star ($\rho = 6 \times 10^{-10}\ gcm^{-3}$, $z = 3 \times 10^{11}\ cm$, $v_{th} = 10^5\ cms^{-1}$) gives a settling speed $v_{settle} \sim 0.06\ cms^{-1}$ and the settling time given by,

$$t_{settle} = \frac{z}{|v_{settle}|} \quad . \tag{2.45}$$

is about $1.5 \times 10^5\ yrs$ (adopted from Armitage, 2020). This result suggests that in the absence of turbulence, the dust particles would settle towards the mid-plane of the disk at a quicker rate.

Settling in the turbulent disk

The presence of turbulence in the disk disturbs small solid particles, preventing them from settling in the mid-plane of the disk. If we consider dust fluid having density, ρ_d as a trace species in the disk ($\frac{\rho_d}{\rho} \ll 1$) then it obeys an advection-diffusion equation:

$$\frac{\partial \rho_d}{\partial t} = D\frac{\partial}{\partial z}\left[\rho \frac{\partial}{\partial z}\left(\frac{\rho_d}{\rho}\right)\right] + \frac{\partial}{\partial z}(\Omega_K^2 t_s \rho_d z) \quad . \tag{2.46}$$

We can obtain a steady-state solutions to this equation if we assume a very thin layer of dust such that the density of gas is approximately constant across the dust scale-height. In this situation, the dimensionless stopping time is independent of z and we obtain,

$$\frac{\rho_d}{\rho} = \left(\frac{\rho_d}{\rho}\right)_{z=0} exp\left[-\frac{z^2}{2h_d^2}\right] \quad , \tag{2.47}$$

where, h_d, the scale-height of the vertical distribution of the dust concentration, $\frac{\rho_d}{\rho}$ is given by,

$$h_d = \sqrt{\frac{D}{\Omega_K^2 t_s}} \quad . \tag{2.48}$$

If we assume the turbulent diffusivity is comparable to the turbulent viscosity, i.e $D \sim \nu$, the ratio of the concentration scale height to the gas scale height can be expressed as,

$$\frac{h_d}{h} \simeq \sqrt{\frac{\alpha}{\tau_s}} \quad . \tag{2.49}$$

Therefore, in order for solid particles to be highly concentrated towards the mid-plane of the disk, the dimensionless stopping time must be significantly larger than α. This suggests that for any reasonable value of α, substantial particle growth is necessary before settling occurs.

Chapter 3

The Model

In order to gain insights into the dynamics of circumprimary disks as well as other protoplanetary disks, it is essential to employ numerical methods for simulating their temporal evolution. This thesis utilizes the FARGO3D code (Benítez-Llambay and Masset, 2016), which is the successor of the FARGO (Fast Advection in Rotating Gaseous Objects) code initially developed by Masset (2000). As the name suggests, the FARGO code utilizes a fast orbital advection algorithm that integrates the motion of gas and solid particles within an orbit. FARGO3D, an extended version of FARGO, also incorporates orbital advection and focuses on describing the characteristics of protoplanetary disks and their interactions with developing planets. It is a versatile and adaptive code specifically designed to run efficiently on clusters of CPUs or GPUs. FARGO3D solves the equations of hydrodynamics (HD) or magnetohydrodynamics (MHD) on a mesh, which can be cartesian, cylindrical, or spherical.

In this section, we will begin by examining the fundamental equations that govern the code, followed by a brief overview of the numerical techniques employed to solve these equations. Lastly, we will present the initial configuration that has been adopted for the simulation.

3.1 Overview of the FARGO3D code

As previously mentioned, FARGO3D is a computational tool that solves the equations of HD or MHD using an Eulerian mesh, which is a grid-based approach. It is primarily designed to handle three-dimensional problems, but it can also be used for one or two dimensions.

3.1.1 Governing equations

The governing equations solved by the FARGO3D code depend on whether it is used for HD or MHD simulations. In this work, we will not address MHD equations as we will not be conducting MHD simulation. We will therefore begin with the continuity equation that describes the conservation of mass in the system and is given by,

$$\frac{\partial \Sigma}{\partial t} + \nabla \cdot (\Sigma \vec{v}) = 0 \quad , \tag{3.1}$$

where, Σ is the surface density and $\vec{v}$ is the velocity of the fluid with respect to the mesh. The Navier-Stokes equation (momentum equation) reads,

$$\Sigma\left(\frac{\partial \vec{v}}{\partial t} + \vec{v}\cdot\nabla\vec{v}\right) = -\nabla P + \nabla\cdot\vec{T} + \vec{F_{ext}} - \Sigma\left[2\vec{\Omega}\times\vec{v} + \vec{\Omega}\times(\vec{\Omega}\times\vec{r}) + \dot{\vec{\Omega}}\times\vec{r}\right] \quad , \tag{3.2}$$

where, P is the pressure, $\vec{F_{ext}}$ is any external force and the final term takes into consideration the potential rotation of the mesh in the vertical axis. The third term incorporates the stress tensor, $\vec{T}$, which represents the internal forces within the fluid and is expressed as follows:

$$\vec{T} = \Sigma\nu\left[\nabla\vec{v} + (\nabla\vec{v})^T - \frac{2}{3}(\nabla\cdot\vec{v})\vec{I}\right] \quad , \tag{3.3}$$

with ν being the kinematic viscosity and $\vec{I}$ being the unit tensor of same rank as the tensor $\nabla\vec{v}$. For the energy equation, we employ a non-conservative form that utilizes the volumetric internal energy, e and is written as,

$$\frac{\partial e}{\partial t} + \nabla \cdot (e\vec{v}) = -P\nabla\cdot\vec{v} \quad , \tag{3.4}$$

In addition, the pressure, P is defined using the ideal gas law:

$$P = R\Sigma T = (\gamma - 1)e \quad , \tag{3.5}$$

where, γ is the adiabatic index, T is the temperature in the midplane of the disk and $R = \dfrac{k_B}{\mu m_u}$ is the universal gas constant with k_B being the Boltzmann constant, μ the mean molecular weight and m_u the unified atomic mass unit. The adiabatic

sound speed c_s within the disk is given by,

$$c_s = \sqrt{\gamma \frac{P}{\Sigma}} = \sqrt{\gamma} c_{s,iso} \quad , \tag{3.6}$$

where, $c_{s,iso} = \sqrt{\frac{P}{\Sigma}}$ is the isothermal sound speed. Furthermore, the vertical scale-height, H reads,

$$H = \frac{c_{s,iso}}{\Omega_K} = \frac{c_s}{\sqrt{\gamma} v_K} r = hr \quad , \tag{3.7}$$

where, Ω_K is the Keplerian angular velocity and h the aspect ratio.

3.1.2 Numerical methods

FARGO3D follows a similar approach to the ZEUS code (Stone and Norman, 1992), where the fluid quantities such as density, internal energy are typically stored at the cell centers. However, the velocities are staggered on the faces of the cells (see Figure 3.1). This arrangement simplifies the calculation of mass, momentum, and specific energy fluxes along the cell edges.

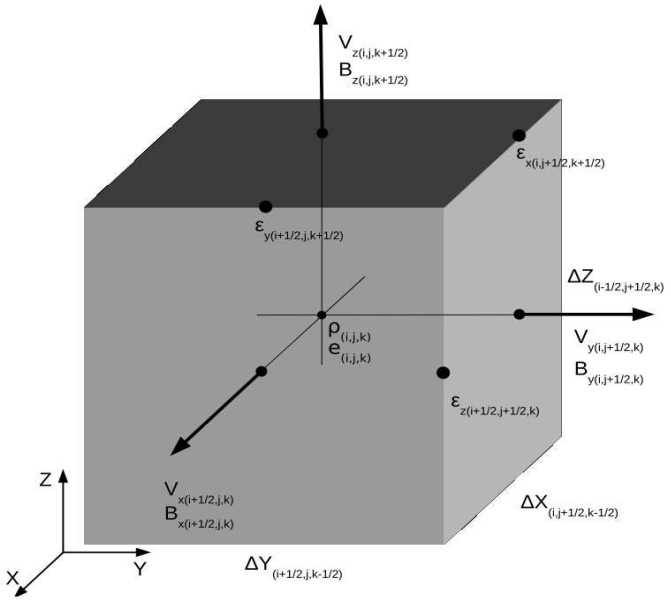

Figure 3.1: A schematic diagram of a cell in FARGO3D (Benítez-Llambay and Masset, 2016).

In particular, FARGO3D solves the hydrodynamical equations using the operator splitting and upwind techniques. Figure 3.2 shows a flow chart of the operations

performed in FARGO3D. Since we will not be considering the magnetic field in this work, we will not address boxes 8, 10, and 11 (see Figure 3.2). We will therefore begin by describing the operator splitting technique that is used to split the HD equations into a source and transport step (boxes 7 and 12 in Figure 3.2).

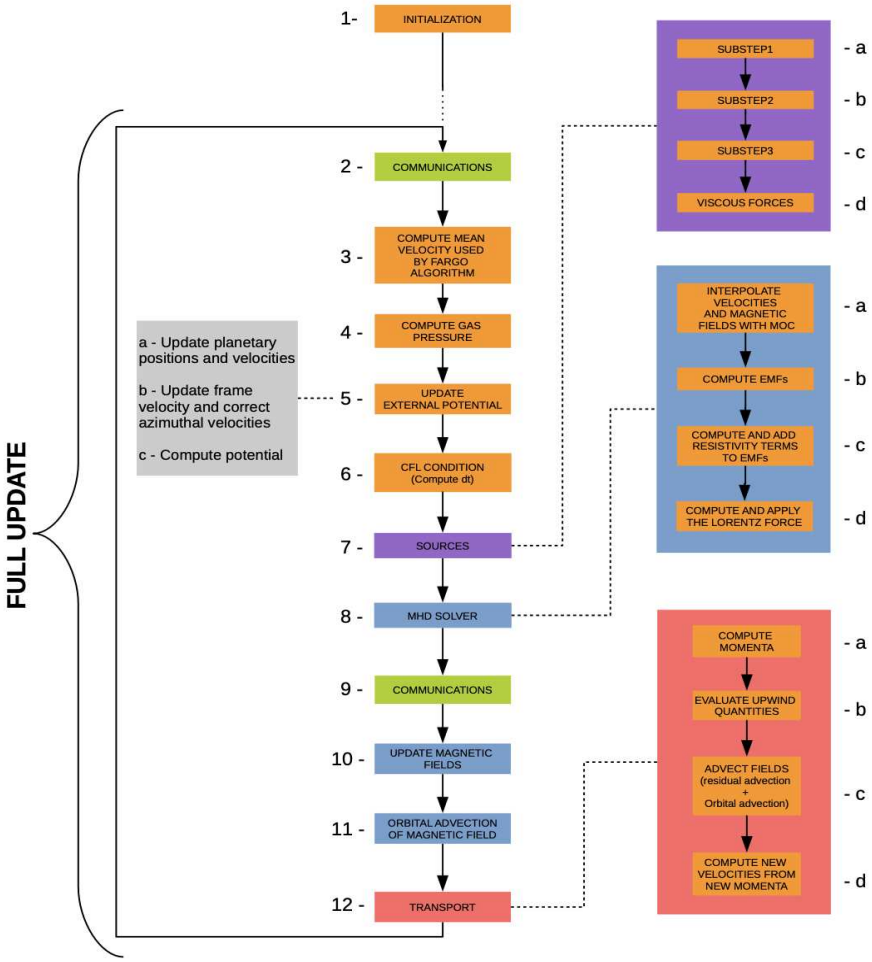

Figure 3.2: A flow chart depicting the sequential operations carried out in FARGO3D during a full update. The boxes with a blue background are exclusive to the MHD case. These corresponding substeps are executed solely when the code is compiled for MHD (Benítez-Llambay and Masset, 2016).

Let us define a equation such that,

$$\frac{\partial U}{\partial t} + A(U) = 0, \quad U(0) = U_0 \quad . \tag{3.8}$$

where, $A(U)$ is a function that can be separated as $A(U) = A_1(U_1) + A_2(U_2)$. Then, its solution can be obtained from the linear combination of the following equations:

$$\frac{\partial U_1}{\partial t} + A_1(U_1) = 0 \quad , \tag{3.9}$$

$$\frac{\partial U_2}{\partial t} + A_2(U_2) = 0 \quad . \tag{3.10}$$

We can now approximate solutions to a differential equation using finite difference scheme, which involves dividing the equation 3.8 into a grid and replacing derivatives with numerical differences between nearby points. For instance,

$$\frac{U_1 - U_0}{\Delta t} = -A_1(U_0) \quad , \tag{3.11}$$

$$\frac{U_2 - U_1}{\Delta t} = -A_2(U_1) \quad . \tag{3.12}$$

We can write the general form of the differential equation in hydrodynamics as,

$$\frac{\partial Q}{\partial t} + \nabla \cdot (Q\vec{v}) = S(Q, \vec{v}, t) \tag{3.13}$$

where, Q can be any vectorial quantity (such as a momentum component) and S are source terms of Q (like a body force). We can now split equation 3.13 into two partial equations using operator splitting technique and can be written as,

$$\textbf{Source step:} \qquad \frac{\partial Q}{\partial t} = S(Q, \vec{v}, t) \tag{3.14}$$

$$\textbf{Transport step:} \qquad \frac{\partial Q}{\partial t} + \nabla \cdot (Q\vec{v}) = 0 \tag{3.15}$$

A transport step involves a series of routines that solves equation 3.15 on the mesh for any given quantity Q. On the other hand, during the source step, all factors that are not included in the transport step need to be taken into account in solving equation 3.14.

In particular, the source step can be linked with the centrifugal force, the pressure gradient, the body forces and the work done by pressure forces. Following the

procedure described by Stone and Norman (1992), the source step can be divided into three sub-steps:

Sub-step 1: It is responsible for updating the velocity field by pressure gradients and gravitational forces.

Sub-step 2: Here, an aritificial viscosity is added along with the heating term.

Sub-step 3: If the energy equation 3.4 is calculated, the workdone by pressure forces is included.

In the transport step, we start solving equation 3.15 by expressing it in the integral form using the divergence theorem as,

$$\frac{\partial}{\partial t}\int\int\int_V Q dV + \int\int_{\partial V} Q\vec{v}\cdot d\vec{S} = 0 \quad , \tag{3.16}$$

assuming that the control volume V is independent of time. This means that the change in Q within a control volume V is solely due to its flux across the boundary ∂V. For multidimensional advection, the transport step is broken down into several one-dimensional problems using finite difference, each updating a portion of the field with the corresponding fluxes, as,

$$\left[Q^{n+a}_{ijk} - Q^{n}_{ijk}\right]V = -\Delta t\left[F_{X\,i+1/2jk} - F_{X\,i-1/2jk}\right]^{n+1/2} \quad , \tag{3.17}$$

$$\left[Q^{n+b}_{ijk} - Q^{n+a}_{ijk}\right]V = -\Delta t\left[F_{Y\,ij+1/2k} - F_{Y\,ij-1/2k}\right]^{n+1/2} \quad , \tag{3.18}$$

$$\left[Q^{n+1}_{ijk} - Q^{n+b}_{ijk}\right]V = -\Delta t\left[F_{Z\,ijk+1/2} - F_{Z\,ijk-1/2}\right]^{n+1/2} \quad , \tag{3.19}$$

where V is the volume of the cell and F is the flux of Q across the faces of the cubic cell. The subscripts (i, j, k) and superscripts $(n + a,\ n + b)$ represents the position of the cell in the grid and intermediate stages of Q respectively. Here, the flux evaluation is done using an upwind method to determine the value of Q^* at the center of the face at a half time step. The flux calculation is simplified by considering

the staggering of the velocity field and is given by,

$$F_{X\,i+1/2}^{n+1/2} = v_{X\,i+1/2}\left[Q_{i+1/2}^{*x}\right]^{n+1/2} S_{i+1/2} \quad , \tag{3.20}$$

where, Q^* is the interpolated value of the cell centered quantity Q onto the face $i+1/2$, at the middle of the time step and the subscript X represent the direction normal to the face along which the flux is evaluated. It is obtained through a zone-wise linear reconstruction technique that utilizes van Leer's slopes (Van Leer, 1977) in most of the sub-steps (with one exception). During the uniform residual step of orbital advection, which will be discussed later, a zone-wise parabolic reconstruction method known as the Piece-wise Parabolic Advection (PPA) algorithm is employed. This approach is similar to the one used in the PLUTO code (Mignone et al., 2012). Furthermore, the interpolated values of density, energy and momenta are evaluated at half time step using van Leer's slope. This sub-step corresponds to the box 12*b* of Figure 3.2.

For transporting momenta-like quantities on a staggered mesh, two versions of each momentum is defined: the left and right momenta, which can be expressed as:

$$\Pi_i^- = \rho_i v_{i-1/2} \tag{3.21}$$

$$\Pi_i^+ = \rho_i v_{i+1/2} \quad , \tag{3.22}$$

Equations 3.21 and 3.22 relate to the product of the cell-centered density, ρ_i and the left interface value of velocity, $v_{i-1/2}$, for the left momenta, as well as the right interface value of velocity, $v_{i+1/2}$, for the right momenta. These momenta are treated as cell-centered quantities during the transport process and are evaluated at the beginning of the transport sub steps, which corresponds to cell 12*a* of Figure 3.2. After completing the transport sub steps, the new velocity is determined based on the updated momenta and density as follows:

$$v_{i-1/2}^{n+1} = \frac{\Pi_{i-1}^{+\,n+1} + \Pi_i^{-n+1}}{\rho_{i-1}^{n+1} + \rho_i^{n+1}} \quad . \tag{3.23}$$

This transformation corresponds to box 12*d* of Figure 3.2. In the case of Carte-

sian coordinates, equations 49 and 50 are applied as stated. However, for different geometries, these equations are adjusted according to Table 3.1.

Table 3.1: Quantities transported in X, Y and Z for different geometries.

Geometry	X-momentum	Y-momentum	Z-momentum
Cartesian	ρv_x	ρv_y	ρv_z
Shearing sheet	$\rho(v_x + 2\Omega_f y)$	ρv_y	ρv_z
Cylindrical	$\rho(r v_\phi + r^2\Omega_f)$	ρv_r	ρv_z
Spherical	$\rho(r v_\phi sin\theta + r^2 sin^2\theta\Omega_f)$	ρv_r	$\rho r v_\theta$

During the transport step, the angular momentum is conserved to machine accuracy and satisfies shock jump conditions, even in the presence of a rotating frame and artificial viscosity. In addition, the code accurately captures the production of vortensity when a fluid passes through a shock (Lin and Papaloizou, 2010). The Courant-Friedrichs-Levy (CFL) condition, also known as the Courant condition, imposes a limit on the integration time step (Δt) over which a full cycle of hydrodynamical sub-steps is performed to maintain stability. In simpler terms, it states that information or changes in the system cannot propagate across more than one cell per time step. Following Stone and Norman (1992), the maximum time step allowed is,

$$\Delta t = C\text{min}\left\{\left(\sum_i \Delta t_i^{-2}\right)^{-1/2}\right\} \quad . \tag{3.24}$$

where, C is called the Courant number. Typically, the value of C is set to 0.44, which is considered a favorable balance between computational speed and stability when dealing with the test problems. Moreover, the different Δt values are associated with distinct processes such as propagation of sound waves, fluid motion, viscosity and resistivity. These processes individually impose limitations on the time step. To address the issue of large nearly uniform azimuthal velocities limiting the time step in the transport step, FARGO3D adopts an orbital advection technique. This technique decomposes the azimuthal velocity into a large, uniform component and a smaller residual component, operating within a nearly corotating frame for each cell ring. The fractional uniform advection is then performed using Piecewise Parabolic Advection, a higher-order interpolation method. Additionally, to enable data synchronization and boundary conditions, an extra layer of ghost or buffer zones is introduced outside the mesh. By utilizing the orbital advection algorithm, which includes circular permutation of indices and conservative updates based on

azimuthal fluxes, FARGO3D ensures the high-accuracy conservation of the fields in the simulation.

Additionally, the FARGO3D code is capable of simulating planetary systems by incorporating point-like masses that interact with the surrounding gas. It employs the fifth-order Cash-Karp method (Cash and Karp, 1990), a fixed time step Runge-Kutta integration scheme based on the CFL condition. For planetary systems without close encounters, the Cash-Karp method provides sufficient accuracy. However, in cases where more precision is required, the code allows for sub-cycling the planetary integration using an adaptive time step decoupled from the CFL condition. The force exerted by the gas on the planets is calculated once per hydrodynamical time step and is utilized to update the planetary velocities. The update of the planetary positions and velocities occurs in cell $5a$ of Figure 3.2.

3.2 Initial conditions

To study the evolution of the gas and dust in circumprimary disk in the presence of a secondary star, we conducted simulations using the new version of the FARGO3D code (Benítez-Llambay et al., 2019). This code has been specifically designed to handle the momentum transfer between the gas and each dust species individually, while neglecting interactions among different dust species. Our focus lies in simulating the dynamics of gas and multiple dust species in the linear drag regime, where the dominant drag mechanism is Epstein drag. The drag force experienced by each dust species is given by,

$$F_{drag} = -\rho_d \frac{\Omega_K}{\tau_s}(v_{dust} - v_{gas}) \quad , \tag{3.25}$$

with ρ_d being the dust density, τ_s the Stokes number of the particle and Ω_K the Keplerian frequency of the gas molecules. The drag coefficient in the above equation 3.25 is included into τ_s. In order to incorporate the diffusion of the dust species within the gas molecules, a new term is added to the continuity equation (Morfill and Völk, 1984), as,

$$\frac{\partial \rho_d}{\partial t} = \nabla \cdot \left(D \rho \nabla \frac{\rho_d}{\rho} \right) \quad , \tag{3.26}$$

where, $\rho = \rho_d + \rho_g$ with ρ_g being the gas density and D the diffusion coefficient, which is considered to be same for all dust species. The initial version of the code

utilized constant values for Stokes numbers, represented as τ_s, in equation 3.26. However, the code has been modified to enable the individual selection of the dust species based on particle size, rather than relying on a fixed Stokes number.

3.2.1 The disk setup

For our simulations we constructed a standard reference model using the physical parameter of the γ Cephei system. We consider that there is no gravitational feedback from the disk onto the stars and neglect the gravitational back-reaction from the disks onto the binary stars. To model the circumprimary disk, we assume that the entire system consisting of the main star, its surrounding disk, and the secondary star is aligned in a single plane. Therefore, the code solves the hydrodynamical equations using polar coordinate system (r, ϕ) centered on the primary star, with the disk residing in the $z = 0$ plane. Additionally, the orbit of the binary is integrated with a fifth-order Runge-Kutta method.

The disk extends from 0.4 to 12 AU and is divided into a grid consisting of 512 elements in the radial direction and 1024 elements in the azimuthal direction, resulting in a total of $524,288$ cells. We employ a power law: $T \propto r^{-1}$ to determine the initial temperature distribution of the disk, which leads to a constant aspect ratio (h) of 0.03. Similarly, for the initial surface density distribution of the gas disk, we consider the power law:

$$\Sigma(r) = \Sigma_0 \left(\frac{r_0}{r} \right) \tag{3.27}$$

where, $\Sigma_0 = 760\ g/cm^2$ is the gas surface density at $r_0 = 1\ AU$. In our simulation, we include three separate groups of dust species with particle sizes of 100 μm, 1 mm, and 1 cm. Each of these dust species has an initial dust-to-gas mass ratio of 0.0033, so that the overall dust-to-gas mass ratio adds up to 0.01. In this model, we adopt a constant value of kinematic viscosity, ν, to be 10^{-5}. Finally, the physical and numerical parameters of our model are summarized in Table 3.2.

Table 3.2: Physical and numerical parameters of our model

Parameter	Value
Mass of the primary star	1.3 $M_{\odot}$
Mass of the secondary star	0.286 $M_{\odot}$
Semi-major axis (a)	20 AU
Eccentricity (e)	0.4
Orbital period (P)	78.85 yrs
α[3]	0.01
Aspect ratio (h)	0.03
Cylindrical mesh ($N_r \times N_\phi$)	512×1024
Total number of time step (N_{tot})	100000000
Time step length (Δt)	0.314159265359
Time step between output (N_{interm})	1000
Uniform kinematic viscosity (ν)	10^{-5}
Damping Zone	1.15
Characteristic time for damping (τ_{damp})	0.3
Inner radius (R_{in})	0.4 AU
Outer radius (R_{out})	12.0 AU
Dust-to-gas mass ratio (ϵ)	0.0033

[3] α is a dimensionless quantity referred to as the Shakura-Sunyaev α parameter. It quantifies the effectiveness of turbulence-induced angular momentum transfer (Shakura and Sunyaev, 1973).

Chapter 4

Results and Discussion

In this particular study, we delve into the intriguing evolution of gas and various dust species (100μm, 1mm, and 1cm) within the circumprimary disk of the γ Cephei system, with a focus on two distinct orbital configurations of the secondary star. Firstly, we explore the highly perturbing configuration when the secondary star is at the pericenter, and secondly, we investigate the less perturbing configuration when it reaches the apocenter. In these two configurations, we investigate how the surface density of the disk evolves with time and compute the mass accretion rate, a critical parameter governing the evolution of the protoplanetary disk and planet formation. To achieve this, we employ the FARGO3D code, as discussed in the previous section 3.1, to conduct a detailed simulation (starting from 0 kyr to 108 kyr) using the parameters presented in Table 3.2. In this chapter, we present and discuss the results obtained from these simulations.

4.1 Surface density evolution

We start by analysing the surface density evolution of three types of dust species (100μm, 1mm, and 1cm) followed by the gas evolution as a function of radius and time.

4.1.1 Dust and gas evolution

Figure 4.1 and 4.2 show the one-dimensional density profiles of the gas and dust particles at different times, illustrating their variations depending on the orbital configuration of the secondary star.

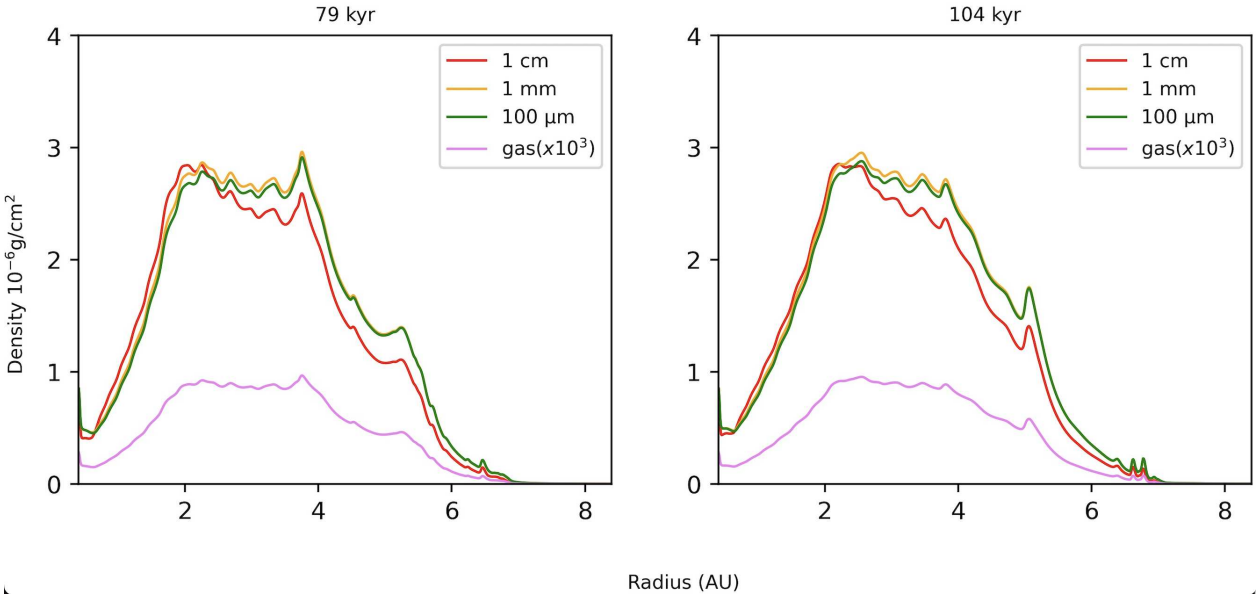

Figure 4.1: The figure displays one-dimensional density profile of gas and three differently-sized dust particles at subsequent times when the secondary star passes through the pericenter.

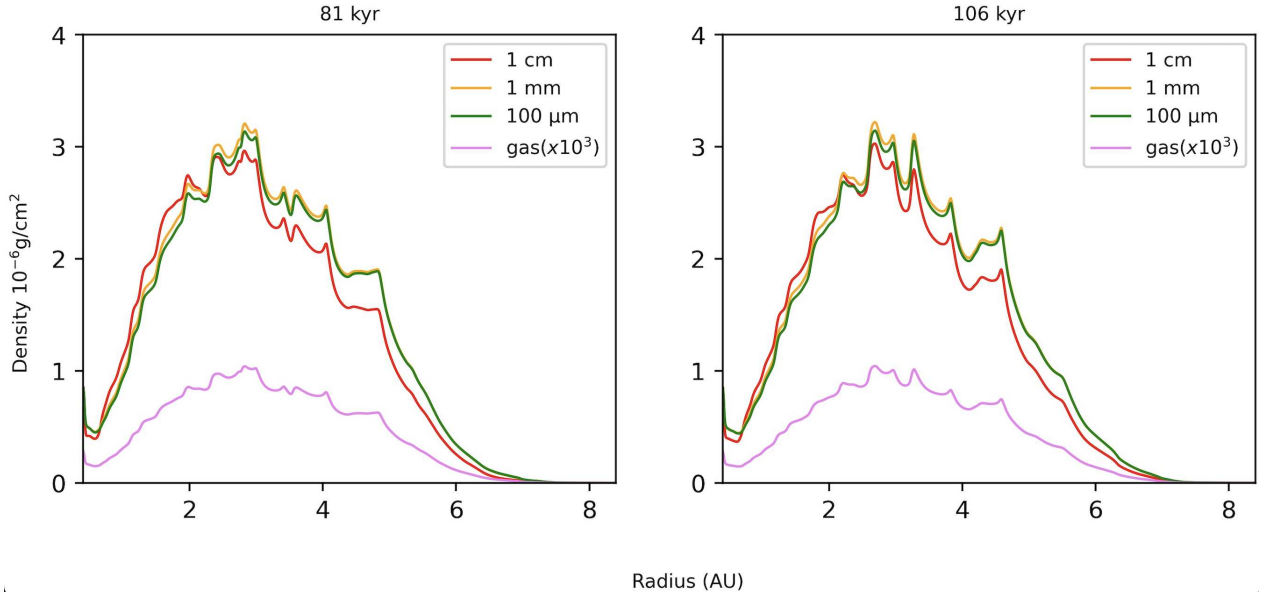

Figure 4.2: The figure displays one-dimensional density profile of gas and three differently-sized dust particles at subsequent times when the secondary star reaches the apocenter.

In Figure 4.3 and 4.4, the two-dimensional density distribution of three different dust species (100μm,1mm, 1cm) is presented at subsequent times, specifically during the secondary star's pericenter and apocenter passages, respectively.

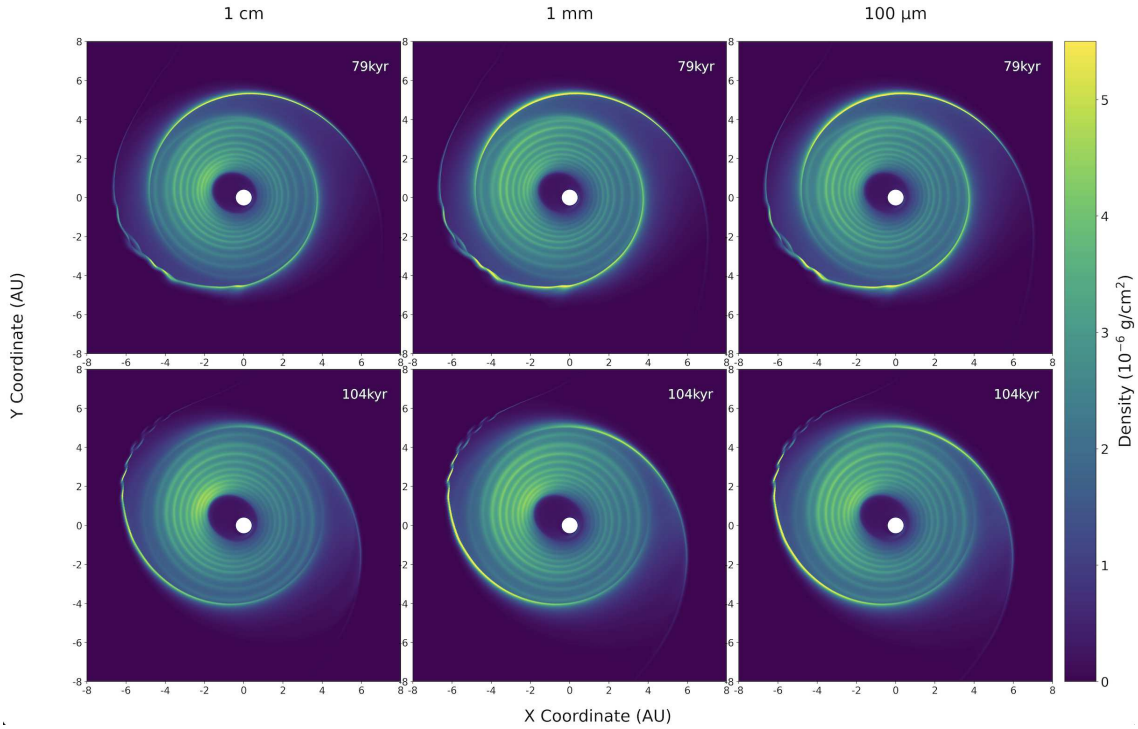

Figure 4.3: The figure illustrates two-dimensional density evolution of the three differently-sized dust particles as a function of time and radius when the secondary star passes through the pericenter. We note two distinct spiral arms induced due to intense tidal forces from the secondary star.

Upon observing these figures, a clear trend emerges: when the secondary companion is at the pericenter, the protoplanetary disk is significantly perturbed as it experiences intense tidal forces. This perturbation gives rise to two prominent and strong spiral arms within the disk structure. As time progresses and the secondary star moves toward the apocenter, the tidal forces weaken, and the disk transitions towards an axisymmetric configuration, damping the spiral arms. Similar trend is observed in the case of the evolution of the gas surface density. Figure 4.5 illustrates the two-dimensional density distribution of gas at different times when the secondary companion passes through the pericenter and reaches the apocenter.

Another interesting thing to note is the presence of over-dense regions within the spiral arms. Within these regions, dust particles have a higher probability of colliding and sticking together due to their increased concentration. These collisions facilitate coagulation, where smaller dust grains merge to form larger aggregates,

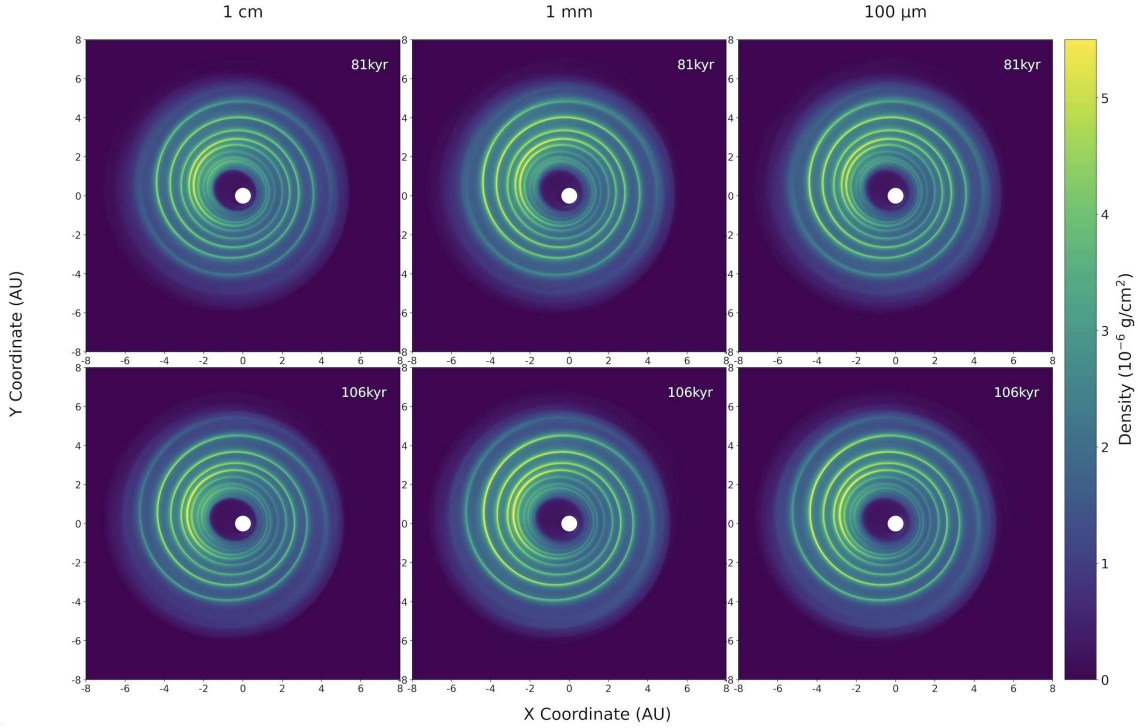

Figure 4.4: The figure illustrates two-dimensional density evolution of the three differently-sized dust particles as a function of time and radius when the secondary star reaches the apocenter. We notice that the spiral arms observed during the pericenter passage of the secondary star dampens out, creating an axisymmetric structure.

creating a favorable environment for the process of accelerated dust growth into larger bodies such as pebbles and planetesimals.

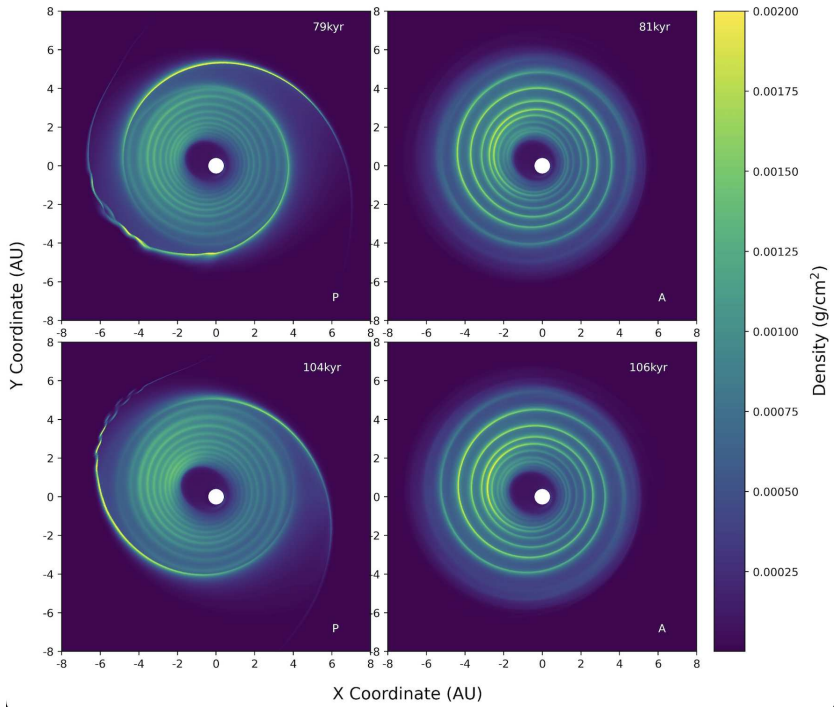

Figure 4.5: The figure shows two-dimensional density evolution of the gas as a function of time and radius when the secondary star passes through the pericenter (P) and reaches the apocenter (A).

4.2 Mass-accretion rate onto the star

While computing the mass accretion rate onto the primary star, we only consider the disk from 2 to 7 AU to be reliable. Within 2 AU, there is the formation of the so-called elliptical hole when simulating binaries. In particular, when gas particles in a disk are on elliptic orbits and pass through the pericenter, they may also cross the inner edge of the grid and become lost. This process leads to the formation of a central elliptic region of low density (Marzari et al., 2009). In addition, we only take into account the gas distribution when considering the mass-accretion rate, as the mass of the gas is 100 times that of the dust particles.

Figure 4.6 and 4.7 present the mass-accretion rate onto the primary star at different times when the secondary star is at the pericenter and apocenter, respectively. The left panel of both figures shows the incoming mass (blue line) and the outgoing mass (red line) moving toward and away from the primary star, respectively. The right panel portrays the total mass-accretion rate on the star (green line), depending on the orbital configuration of the secondary star.

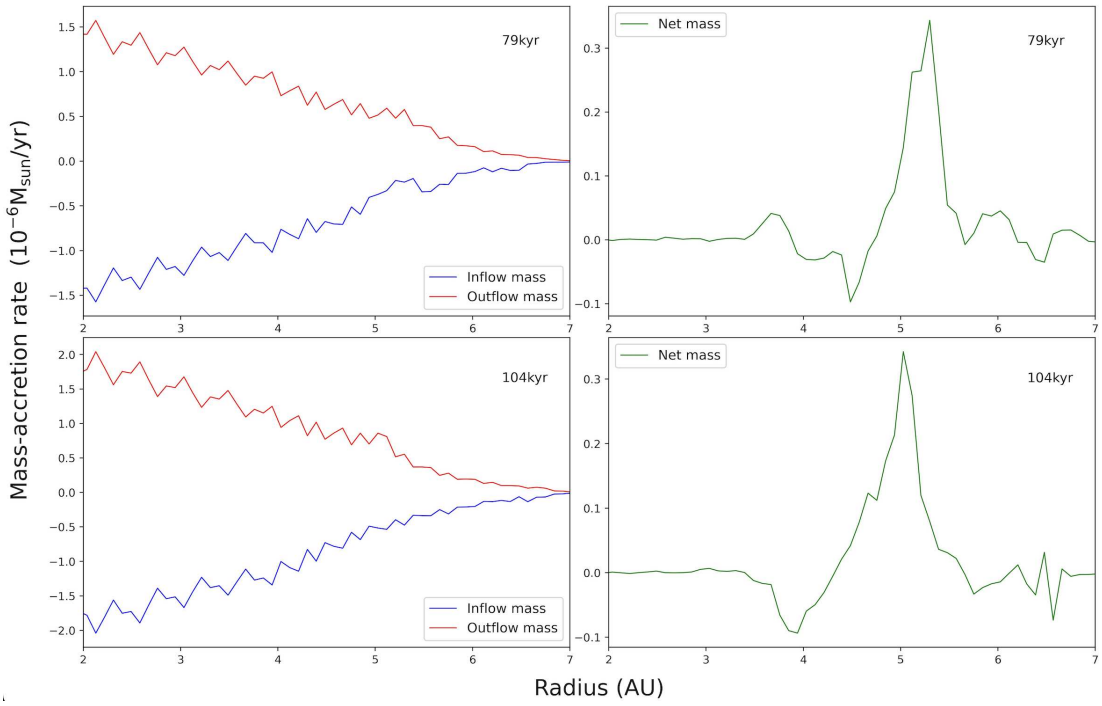

Figure 4.6: Left panel: The figure displays the mass-accretion rate towards (blue line) and away (red line) from the primary star at the secondary star's pericenter passage. Right panel: The figure illustrates the net mass-accretion rate onto the primary star at the pericenter.

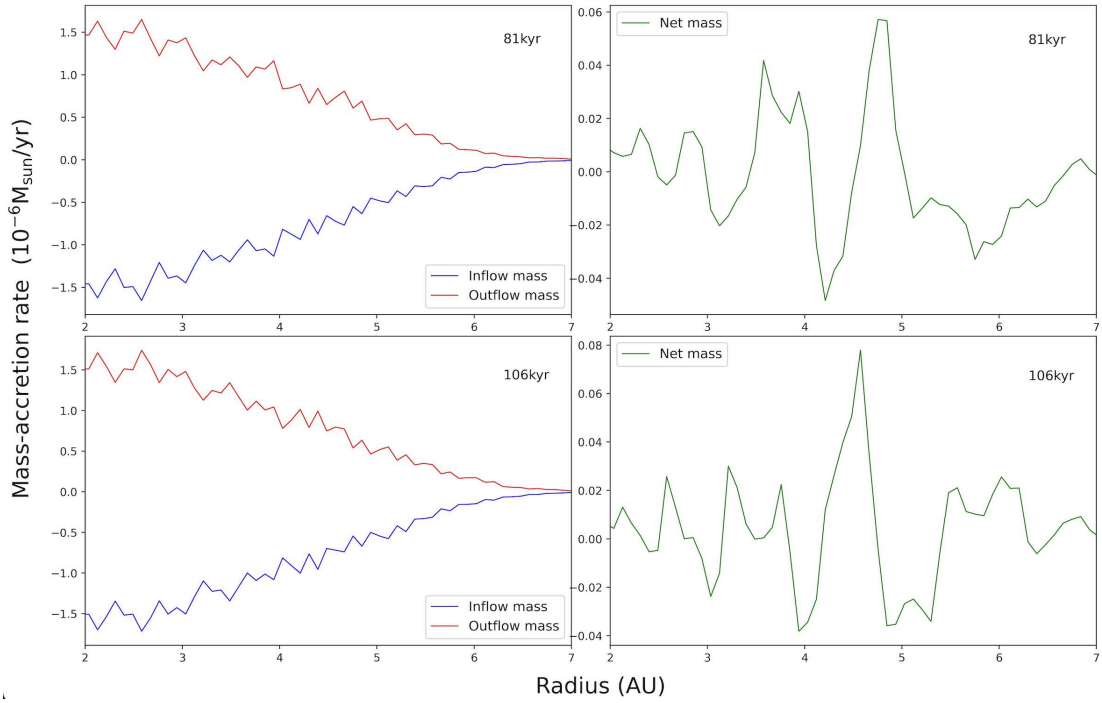

Figure 4.7: Left panel: The figure displays the mass-accretion rate towards (blue line) and away (red line) from the primary star at the secondary star's apocenter passage. Right panel: It illustrates the net mass-accretion rate onto the primary star at the apocenter.

We obtain the total mass-accretion rate to be $1.224 \times 10^{-6}\ M_{sun}/yr$ at 79kyr and $9.231 \times 10^{-7}\ M_{sun}/yr$ at 104kyr when the secondary star passes through the pericenter. Additionally, when the star reaches the apocenter, we obtain the total mass-accretion rate to be $-1.408 \times 10^{-7}\ M_{sun}/yr$ at 81kyr and $1.729 \times 10^{-7}\ M_{sun}/yr$ at 106kyr.

Furthermore, we can notice from the Figure 4.6 that when the secondary star passes through the pericenter, the total mass-accretion rate increases at around 4.5 to 5.5 AU. This clearly indicates that the mass is dragged away by the spiral waves (see Figure 4.5). And, when the secondary star is at the apocenter, the viscous mass accretion dominates, leading mass to the primary star.

Moreover, the drag forces from the spiral waves could be strong enough to open a gap in the disk at the pericenter, which, in turn, can significantly affect the disk's dynamics. Additionally, these spiral waves could possibly redistribute the material in the disk, moving it from the inner to the outer regions. This redistribution has the potential to alter the distribution of material available for planet formation and, consequently, influence the formation and evolution of planets. Furthermore, the viscous mass accretion that dominates at the apocenter has the potential to

generate radiation that heats and ionizes the disk, leading to photoevaporation and mass loss. The combination of the drag forces from spiral waves at the pericenter and viscous accretion dominating at the apocenter can also lead to disk truncation, leaving less material for planets to form.

However, we need to carry out further detailed simulations and observations to fully comprehend the impact of these effects on circumprimary disks and planet formation in close binaries.

4.2.1 Weighted mass-accretion rate

We also performed calculations involving the mass-accretion rate, considering the mass of the local ring, to gain valuable insights into the specific region of the circumprimary disk. This rate refers to the rate at which material accumulates or accretes onto a particular region or ring within the larger system, while taking into account the mass distribution within that ring. Moreover, protoplanetary disks often display intricate structures like gaps and rings, leading to variations in the accretion process at different radial distances. By incorporating the mass of the local ring, the mass-accretion rate allows us to resolve such variations, where the accretion rate may be either higher or lower than the global disk average rate, facilitating a more detailed and localized analysis of the accretion process.

Figure 4.8 shows the mass-accretion rate weighted with the mass of the local ring at different times, both when the secondary star is at the pericenter and when it reaches the apocenter, respectively. In Figure 4.8, we can observe negative values dominating for weighted mass-accretion rate at around 4.5 to 5.5 AU during the secondary star's pericenter passage. This indicates that material is getting accreted onto a local ring at around 4.5 to 5.5 AU. This clearly agrees with the trend observed in the case of the total mass-accretion rate at both the pericenter and apocenter passage of secondary star.

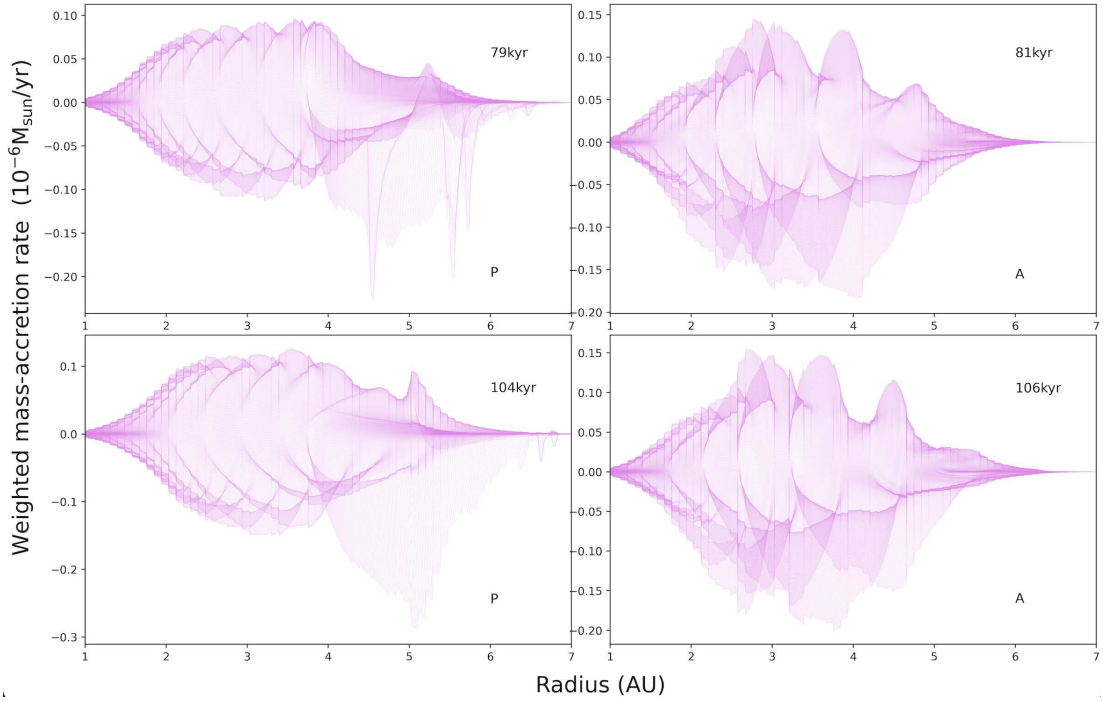

Figure 4.8: The figure illustrates the mass accretion rate weighted with the mass of the local ring as a function of time and radius at the secondary star's pericenter passage (left column) and apocenter passage (right column).

Chapter 5

Conclusion and Outlook

Despite the detection of dozen of planets in close binaries, how did those planets form in such close proximity is still an open question to discuss. The planet formation process in binaries is believed to occur in series of complex stages, each of these stages can be altered differently by the presence of the secondary star.

Our research presents a significant advancement in the understanding of early stage planet formation within the circumprimary disk of close binaries. Through comprehensive hydrodynamical simulations, we have identified crucial patterns in the evolution of the disk dynamics, driven by the presence of the secondary star. At the pericenter of the secondary star, intense tidal forces induce notable perturbations, resulting in the emergence of two distinct and strong spiral waves within the disk. As the secondary star proceeds towards the apocenter, the diminishing tidal effects prompt the disk to transition into an axisymmetric state, causing the gradual damping of the spiral arms.

Of particular importance is the observed over-dense regions within the spiral arms formed during the pericenter passage. This enhanced concentration of dust particles fosters their collisions and cohesion, promoting coagulation of smaller grains into larger aggregates. This process provides favorable environment for the accelerated dust growth, eventually leading to the formation of pebbles and planetesimals.

Moreover, we obtained the total mass-accretion rate to be $1.224 \times 10^{-6}\ M_{sun}/yr$ at 79kyr and $9.231 \times 10^{-7}\ M_{sun}/yr$ at 104kyr when the secondary star passes through the pericenter and at the apocenter, we obtained the total mass-accretion rate to be $-1.408 \times 10^{-7}\ M_{sun}/yr$ at 81kyr and $1.729 \times 10^{-7}\ M_{sun}/yr$ at 106kyr.

Notably, our analysis of the mass-accretion rate onto the primary star reveals intriguing insights into mass transfer mechanisms. During the secondary star's pericenter passage, the spiral waves efficiently drag mass away from the disk, resulting

in mass loss. Conversely, during the apocenter passage, viscous mass accretion dominates, driving mass onto the primary star. Remarkably, these accretion patterns align closely with regions where spiral waves are observed, indicating a clear correlation between disk perturbations and mass accretion.

Our research significantly contributes to the broader understanding of planet formation in binary star systems. The intricate interplay between stellar companions and circumprimary disks during the early stages of planet formation emerges as a critical factor in shaping planetary architectures. These findings provide valuable insights into the complexities of planetary system evolution and pave the way for further exploration and refinement of theoretical models.

In summary, our investigation sheds light on the intriguing interactions between binary systems and the planet formation process. By uncovering the mechanisms that govern this interplay, our research contributes to the ongoing quest for a deeper understanding of planetary system formation across the cosmos.

Bibliography

Andre, P. (2000). The initial conditions for protostellar collapse: Observational constraints. Technical report, SIS-2002-162.

Ansdell, M., Williams, J., Trapman, L., van Terwisga, S., Facchini, S., Manara, C., van der Marel, N., Miotello, A., Tazzari, M., Hogerheijde, M., et al. (2018). Alma survey of lupus protoplanetary disks. ii. gas disk radii. *The Astrophysical Journal*, 859(1):21.

Apai, D., Pascucci, I., Brandner, W., Henning, T., Lenzen, R., Potter, D., Lagrange, A.-M., and Rousset, G. (2004). Naco polarimetric differential imaging of tw hya-a sharp look at the closest t tauri disk. *Astronomy & Astrophysics*, 415(2):671–676.

Armitage, P. J. (2020). *Astrophysics of planet formation*. Cambridge University Press.

Armitage, P. J. and Kley, W. (2019). *From Protoplanetary Disks to Planet Formation*. Springer.

Artymowicz, P. and Lubow, S. H. (1994). Dynamics of binary-disk interaction. 1: Resonances and disk gap sizes. *The Astrophysical Journal*, 421:651–667.

Benítez-Llambay, P., Krapp, L., and Pessah, M. E. (2019). Asymptotically stable numerical method for multispecies momentum transfer: gas and multifluid dust test suite and implementation in fargo3d. *The Astrophysical Journal Supplement Series*, 241(2):25.

Benítez-Llambay, P. and Masset, F. S. (2016). Fargo3d: a new gpu-oriented mhd code. *The Astrophysical Journal Supplement Series*, 223(1):11.

Beuzit, J.-L., Feldt, M., Dohlen, K., Mouillet, D., Puget, P., Wildi, F., Abe, L., Antichi, J., Baruffolo, A., Baudoz, P., et al. (2008). Sphere: a planet finder instrument for the vlt. In *Ground-based and airborne instrumentation for astronomy II*, volume 7014, pages 476–487. SPIE.

Blandford, R. D. and Payne, D. (1982). Hydromagnetic flows from accretion discs and the production of radio jets. *Monthly Notices of the Royal Astronomical Society*, 199(4):883–903.

Bohlin, R. C., Savage, B. D., and Drake, J. (1978). A survey of interstellar hi from l-alpha absorption measurements. ii. *Astrophysical Journal, Part 1, vol. 224, Aug. 15, 1978, p. 132-142. Research supported by the Lockheed Independent Research Program;*, 224:132–142.

Bonavita, M. and Desidera, S. (2007). The frequency of planets in multiple systems. *Astronomy & Astrophysics*, 468(2):721–729.

Bromley, B. C. and Kenyon, S. J. (2015). Planet formation around binary stars: Tatooine made easy. *The Astrophysical Journal*, 806(1):98.

Campbell, B., Walker, G. A., and Yang, S. (1988). A search for substellar companions to solar-type stars. *The Astrophysical Journal*, 331:902–921.

Cash, J. R. and Karp, A. H. (1990). A variable order runge-kutta method for initial value problems with rapidly varying right-hand sides. *ACM Transactions on Mathematical Software (TOMS)*, 16(3):201–222.

Correia, A., Udry, S., Mayor, M., Eggenberger, A., Naef, D., Beuzit, J.-L., Perrier, C., Queloz, D., Sivan, J.-P., Pepe, F., et al. (2008). The elodie survey for northern extra-solar planets-iv. hd 196885, a close binary star with a 3.7-year planet. *Astronomy & Astrophysics*, 479(1):271–275.

Deck, K. M., Payne, M., and Holman, M. J. (2013). First-order resonance overlap and the stability of close two-planet systems. *The Astrophysical Journal*, 774(2):129.

Desidera, S. and Barbieri, M. (2007). Properties of planets in binary systems-the role of binary separation. *Astronomy & Astrophysics*, 462(1):345–353.

Duchêne, G. (2010). Planet formation in binary systems: a separation-dependent mechanism? *The Astrophysical Journal Letters*, 709(2):L114.

Dullemond, C. and Monnier, J. (2010). The inner regions of protoplanetary disks. *Annual Review of Astronomy and Astrophysics*, 48:205–239.

Dullemond, C., Natta, A., and Testi, L. (2006). Accretion in protoplanetary disks: The imprint of core properties. *The Astrophysical Journal*, 645(1):L69.

Dumusque, X., Pepe, F., Lovis, C., Ségransan, D., Sahlmann, J., Benz, W., Bouchy, F., Mayor, M., Queloz, D., Santos, N., et al. (2012). An earth-mass planet orbiting α centauri b. *Nature*, 491(7423):207–211.

Eggenberger, A., Udry, S., Chauvin, G., Beuzit, J.-L., Lagrange, A.-M., Ségransan, D., and Mayor, M. (2007). The impact of stellar duplicity on planet occurrence and properties-i. observational results of a vlt/naco search for stellar companions to 130 nearby stars with and without planets. *Astronomy & Astrophysics*, 474(1):273–291.

Ginski, C., Stolker, T., Pinilla, P., Dominik, C., Boccaletti, A., De Boer, J., Benisty, M., Biller, B., Feldt, M., Garufi, A., et al. (2016). Direct detection of scattered light gaps in the transitional disk around hd 97048 with vlt/sphere. *Astronomy & Astrophysics*, 595:A112.

Haghighipour, N. (2006). Dynamical stability and habitability of the γ cephei binary-planetary system. *The Astrophysical Journal*, 644(1):543.

Haghighipour, N. (2011). Super-earths: a new class of planetary bodies. *Contemporary Physics*, 52(5):403–438.

Haghighipour, N. and Kaltenegger, L. (2013). Calculating the habitable zone of binary star systems. ii. p-type binaries. *The Astrophysical Journal*, 777(2):166.

Haghighipour, N. and Raymond, S. N. (2007). Habitable planet formation in binary planetary systems. *The Astrophysical Journal*, 666(1):436.

Hatzes, A. P. (2016). The architecture of exoplanets. *Space Science Reviews*, 205:267–283.

Hatzes, A. P., Cochran, W. D., Endl, M., McArthur, B., Paulson, D. B., Walker, G. A., Campbell, B., and Yang, S. (2003). A planetary companion to γ cephei a. *The Astrophysical Journal*, 599(2):1383.

Hilditch, R. W. (2001). *An introduction to close binary stars*. Cambridge University Press.

Holman, M. J. and Wiegert, P. A. (1999). Long-term stability of planets in binary systems. *The Astronomical Journal*, 117(1):621.

Jang-Condell, H., Mugrauer, M., and Schmidt, T. (2008). Disk truncation and planet formation in γ cephei. *The Astrophysical Journal*, 683(2):L191.

Kaltenegger, L. and Haghighipour, N. (2013). Calculating the habitable zone of binary star systems. i. s-type binaries. *The Astrophysical Journal*, 777(2):165.

Kley, W. and Haghighipour, N. (2014). Modeling circumbinary planets: The case of kepler-38. *Astronomy & Astrophysics*, 564:A72.

Kley, W. and Nelson, R. P. (2008). Planet formation in binary stars: the case of γ cephei. *Astronomy & Astrophysics*, 486(2):617–628.

Kley, W. and Nelson, R. P. (2010). Early evolution of planets in binaries: planet–disk interaction. *Planets in binary star systems*, pages 135–164.

Kuhn, J., Potter, D., and Parise, B. (2001). Imaging polarimetric observations of a new circumstellar disk system. *The Astrophysical Journal*, 553(2):L189.

Libert, A.-S. and Henrard, J. (2005). Analytical approach to the secular behaviour of exoplanetary systems. *Celestial Mechanics and Dynamical Astronomy*, 93:187–200.

Lin, M.-K. and Papaloizou, J. C. (2010). Type iii migration in a low-viscosity disc. *Monthly Notices of the Royal Astronomical Society*, 405(3):1473–1490.

Marois, C., Lafreniere, D., Doyon, R., Macintosh, B., and Nadeau, D. (2006). Angular differential imaging: a powerful high-contrast imaging technique. *The Astrophysical Journal*, 641(1):556.

Martin, D. V. (2018). Populations of planets in multiple star systems. *arXiv preprint arXiv:1802.08693*.

Marzari, F. and Scholl, H. (2000). Planetesimal accretion in binary star systems. *The Astrophysical Journal*, 543(1):328.

Marzari, F., Scholl, H., Thébault, P., and Baruteau, C. (2009). On the eccentricity of self-gravitating circumstellar disks in eccentric binary systems. *Astronomy & Astrophysics*, 508(3):1493–1502.

Marzari, F. and Thebault, P. (2019). Planets in binaries: formation and dynamical evolution. *Galaxies*, 7(4):84.

Marzari, F., Weidenschilling, S., Barbieri, M., and Granata, V. (2005). Jumping jupiters in binary star systems. *The Astrophysical Journal*, 618(1):502.

Masset, F. (2000). Fargo: A fast eulerian transport algorithm for differentially rotating disks. *Astronomy and Astrophysics Supplement Series*, 141(1):165–173.

Michtchenko, T. A. and Malhotra, R. (2004). Secular dynamics of the three-body problem: application to the υ andromedae planetary system. *Icarus*, 168(2):237–248.

Mignone, A., Flock, M., Stute, M., Kolb, S., and Muscianisi, G. (2012). A conservative orbital advection scheme for simulations of magnetized shear flows with the pluto code. *Astronomy & Astrophysics*, 545:A152.

Mizuno, H. (1980). Formation of the giant planets. *Progress of Theoretical Physics*, 64(2):544–557.

Morfill, G. and Völk, H. (1984). Transport of dust and vapor and chemical fractionation in the early protosolar cloud. *The Astrophysical Journal*, 287:371–395.

Mudryk, L. R. and Wu, Y. (2006). Resonance overlap is responsible for ejecting planets in binary systems. *The Astrophysical Journal*, 639(1):423.

Mugrauer, M. and Neuhäuser, R. (2009). The multiplicity of exoplanet host stars-new low-mass stellar companions of the exoplanet host stars hd 125612 and hd 212301. *Astronomy & Astrophysics*, 494(1):373–378.

Müller, T. W. and Kley, W. (2012). Circumstellar disks in binary star systems-models for γ cephei and α centauri. *Astronomy & Astrophysics*, 539:A18.

Naoz, S. (2016). The eccentric kozai-lidov effect and its applications. *Annual Review of Astronomy and Astrophysics*, 54:441–489.

Nelson, A. F. (2000). Planet formation is unlikely in equal-mass binary systems with a˜ 50 au. *The Astrophysical Journal*, 537(1):L65.

Paardekooper, S.-J., Thebault, P., and Mellema, G. (2008). Planetesimal and gas dynamics in binaries. *Monthly Notices of the Royal Astronomical Society*, 386(2):973–988.

Picogna, G. and Marzari, F. (2013). Three-dimensional modeling of radiative disks in binaries. *Astronomy & Astrophysics*, 556:A148.

Pollack, J. B., Hubickyj, O., Bodenheimer, P., Lissauer, J. J., Podolak, M., and Greenzweig, Y. (1996). Formation of the giant planets by concurrent accretion of solids and gas. *icarus*, 124(1):62–85.

Raghavan, D., Henry, T. J., Mason, B. D., Subasavage, J. P., Jao, W.-C., Beaulieu, T. D., and Hambly, N. C. (2006). Two suns in the sky: stellar multiplicity in exoplanet systems. *The Astrophysical Journal*, 646(1):523.

Raghavan, D., McAlister, H. A., Henry, T. J., Latham, D. W., Marcy, G. W., Mason, B. D., Gies, D. R., White, R. J., and Ten Brummelaar, T. A. (2010). A survey of stellar families: multiplicity of solar-type stars. *The Astrophysical Journal Supplement Series*, 190(1):1.

Safronov, V. S. (1972). Evolution of the protoplanetary cloud and formation of the earth and the planets.

Savonije, G., Papaloizou, J., and Lin, D. (1994). On tidally induced shocks in accretion discs in close binary systems. *Monthly Notices of the Royal Astronomical Society*, 268(1):13–28.

Shakura, N. I. and Sunyaev, R. A. (1973). Black holes in binary systems. observational appearance. *Astronomy and Astrophysics*, 24:337–355.

Stone, J. M. and Norman, M. L. (1992). Zeus-2d: a radiation magnetohydrodynamics code for astrophysical flows in two space dimensions. i-the hydrodynamic algorithms and tests. *Astrophysical Journal Supplement Series (ISSN 0067-0049), vol. 80, no. 2, June 1992, p. 753-790. Research supported by University of Illinois.*, 80:753–790.

Thebault, P., Marzari, F., and Scholl, H. (2008). Planet formation in α centauri a revisited: not so accretion friendly after all. *Monthly Notices of the Royal Astronomical Society*, 388(4):1528–1536.

Thebault, P., Marzari, F., and Scholl, H. (2009). Planet formation in the habitable zone of α centauri b. *Monthly Notices of the Royal Astronomical Society: Letters*, 393(1):L21–L25.

Van Leer, B. (1977). Towards the ultimate conservative difference scheme. iv. a new approach to numerical convection. *Journal of computational physics*, 23(3):276–299.

Weidenschilling, S. (1977). Aerodynamics of solid bodies in the solar nebula. *Monthly Notices of the Royal Astronomical Society*, 180(2):57–70.

Zucker, S., Mazeh, T., Santos, N., Udry, S., and Mayor, M. (2004). Multi-order todcor: Application to observations taken with the coralie echelle spectrograph-ii. a planet in the system hd 41004. *Astronomy & Astrophysics*, 426(2):695–698.

Acknowledgements

I want to start by thanking my advisor, Prof. Francesco Marzari. He not only gave me the chance to work on what I love but also spent a lot of time helping me understand things, sharing ideas, and creating new opportunities.

I am really thankful to the Università degli Studi di Padova for guiding me through my studies and helping me grow over the last two years. I can't forget my friends - their constant support means the world to me.

And most importantly, my parents. They have always been there for me, believing in me, and making me who I am today.